PHYSICAL REVIEW D **87,** 082001 (2013)

Brownian thermal noise in multilayer coated mirrors

Ting Hong,[1] Huan Yang,[1] Eric K. Gustafson,[2] Rana X. Adhikari,[2] and Yanbei Chen[1]
[1]*Theoretical Astrophysics 350-17, California Institute of Technology, Pasadena, California 91125, USA*
[2]*LIGO Laboratory 100-36, California Institute of Technology, Pasadena, California 91125, USA*
(Received 16 January 2013; published 2 April 2013)

We analyze the Brownian thermal noise of a multilayer dielectric coating used in high-precision optical measurements, including interferometric gravitational-wave detectors. We assume the coating material to be isotropic, and therefore study thermal noises arising from shear and bulk losses of the coating materials. We show that coating noise arises not only from layer thickness fluctuations, but also from fluctuations of the interface between the coating and substrate, driven by fluctuating shear stresses of the coating. Although thickness fluctuations of different layers are statistically independent, there exists a finite coherence between the layers and the substrate-coating interface. In addition, photoelastic coefficients of the thin layers (so far not accurately measured) further influence the thermal noise, although at a relatively low level. Taking into account uncertainties in material parameters, we show that significant uncertainties still exist in estimating coating Brownian noise.

DOI: 10.1103/PhysRevD.87.082001 PACS numbers: 04.80.Nn, 05.40.−a

I. INTRODUCTION

Brownian thermal noise in the dielectric coatings of mirrors limits some high-precision experiments which use optical metrology. This thermal noise is currently a limit for fixed spacer Fabry-Perots used in optical clock experiments [1] and is estimated to be the dominant noise source in the most sensitive band of modern gravitational-wave detectors (e.g., Advanced LIGO, GEO, Advanced VIRGO and KAGRA) [2–6]. Recent work has indicated the possibility of reducing the various kinds of internal thermal noise by redesigning the shape of the optical mode [7,8] or the structure of the multilayer coating [9,10]. In this paper, we seek a more comprehensive understanding of coating Brownian noise. We first identify all thermally fluctuating physical properties (e.g., different components of the strain tensor) of the coating that can lead to coating Brownian noise, and calculate how each of them contributes (linearly) to the total noise; we then calculate their individual levels of fluctuation, as well as cross correlations between pairs of them, using the fluctuation-dissipation theorem [11–13]. In this way, as we compute the total coating Brownian noise, it will be clear how each factor contributes, and we will be in a better position to take advantage of possible correlations between different components of the noise.

As a starting point, we will assume each coating layer to be isotropic, and hence completely characterized by its complex bulk modulus K and shear modulus μ—each with small imaginary parts related to the energy loss in the bulk and shear motions. The complex arguments of these moduli are often referred to as *loss angles*. While values of K and μ are generally known, loss angles of thin optical layers vary significantly according to the details of the coating process (i.e., how coating materials are applied onto the substrate and their composition). Since the loss angles are small, we will use K and μ to denote the real parts of the bulk and shear moduli, and write the complex bulk and shear moduli, $\tilde{K}$ and $\tilde{\mu}$, as

$$\tilde{K} = K(1 + i\phi_B), \qquad \tilde{\mu} = \mu(1 + i\phi_S). \tag{1}$$

Here we have used subscripts B and S to denote bulk and shear, because these will be symbols for bulk strain and shear strain.

Note that our definition differs from previous literature, which used $\phi_\parallel$ and $\phi_\perp$ to denote losses induced by elastic deformations parallel and perpendicular to the coating-substrate interface [14]. As we shall argue in Appendix C, $\phi_\parallel$ and $\phi_\perp$ cannot be consistently used as independent loss angles of a material. Only assuming $\phi_\parallel = \phi_\perp = \phi_S = \phi_B$ will the previous calculation agree with ours—if we ignore light penetration into the coating. There is, *a priori*, no reason why these loss angles should all be equal, although this assumption has so far been compatible with existing ring-down measurements and direct measurements of coating thermal noise [15].

Brownian thermal fluctuations of a multilayer coating can be divided as follows: (i) thickness fluctuation of the coating layers, (ii) fluctuation of the coating-substrate interface, and (iii) refractive index fluctuations of the coating layers associated with longitudinal (thickness) and transverse (area) elastic deformations—as illustrated in Fig. 1. Using what is sometimes referred to as Levin's direct approach [12] (based on the fluctuation-dissipation theorem) and writing the coating Brownian noise as a linear combination of the above fluctuations allows the construction of a corresponding set of forces acting on the coating and calculation of the thermal noise spectrum from the dissipation associated with the simultaneous application of these forces. This has been carried out by Gurkovsky and Vyatchanin [16], as well as Kondratiev *et al.* [17]. However, in order to obtain insights into coating noise

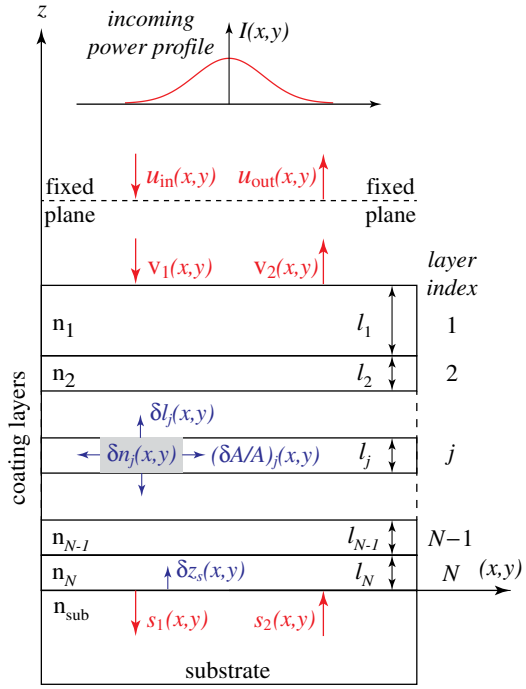

FIG. 1 (color online). Drawing of a mirror coated with multiple dielectric layers. Shown here are the various fluctuations that contribute to coating noise, i.e., fluctuations in the amplitude and phase of the returning light caused by fluctuations in the geometry [including layer thickness δl_j, layer area stretch $(\delta A/A)_j$, and interface height z_s of the coating-substrate configuration] and in the refractive indices $\delta n_j(x, y, z)$ of the layers.

that have proven useful we have chosen to calculate the cross spectral densities for each of (i), (ii), and (iii), and to provide intuitive interpretations of each. We will show, in Sec. IV, that (i) and (ii) above are driven by both bulk and shear fluctuations in the coating, in such a way that thickness fluctuations of the jth layer δl_j, or in transverse locations separated by more than a coating thickness, are mutually statistically independent, yet each δl_j is correlated with the fluctuation of the coating-substrate interface z_s—because z_s is driven by the *sum* of thermal stresses in the coating layers. We will also show that when coating thickness is much less than the beam spot size, the only significant contribution to (iii) arises from longitudinal (thickness) fluctuations; see Appendix A 4 for details.

This paper is organized as follows. In Sec. II, we express the amplitude and phase of the reflected field in terms of fluctuations in the coating structure, thereby identifying the various components of coating thermal noise. In Sec. III, we introduce the loss angles of isotropic coating materials, and use the fluctuation-dissipation theorem to calculate the cross spectral densities of the coating thermal noise, ignoring light penetration into the multilayer coating. In Sec. IV, we discuss in detail the cross spectra of all the components of the coating structure fluctuation, thereby obtaining the full formula for coating thermal noise, taking light penetration within the multilayers into account. The key formulas summarizing the phase and amplitude noise spectrum are given in Eqs. (94) and (95). In Sec. V, we discuss the effect of light penetration on coating thermal noise, using typical optical coating structures. In Sec. VI, we discuss the dependence of thermal noise on the material parameters, and optimize the coating structure in order to lower the thermal noise. In Sec. VII, we discuss how only one combination of the two loss angles has been measured in past experiments, and how other different combinations can be measured using a new experimental geometry. Finally, we summarize our main conclusions in Sec. VIII.

II. COMPONENTS OF THE COATING THERMAL NOISE

In this section, we express the coating thermal noise in terms of the elastic deformations of the coated substrate.

A. Complex reflectivity

As illustrated in Fig. 1, we consider a laser field normally incident (along the $-z$ direction) onto the mirror, with complex amplitude profile $u_{in}(x, y)$ at a fixed reference plane (dashed line in the figure) and intensity profile $I(x, y) = |u_{in}(x, y)|^2$. Henceforth in the paper, we shall use arrows (e.g., $\vec{x}$) to denote the two-dimensional vector (x, y) in the *transverse plane*, and boldface letters (e.g., $\mathbf{x}$) to denote three-dimensional vectors.

Because the coating thickness is much less than the beam spot size, the reflected field (traveling along the $+z$ direction) at transverse location $\vec{x}$ has an amplitude given by

$$u_{out}(\vec{x}) = \rho_{tot}(\vec{x}) u_{in}(\vec{x}), \tag{2}$$

which only depends on the complex reflectivity $\rho_{tot}(\vec{x})$ and the complex amplitude of the incident field $u_{in}(\vec{x})$, at the same location $\vec{x}$—assuming no incident light from the substrate (i.e., $s_2 = 0$). Here $\rho_{tot}(\vec{x})$ can be separated into three factors, as

$$\rho_{tot}(\vec{x}) = \frac{u_{out}(\vec{x})}{u_{in}(\vec{x})} = \left[\frac{u_{out}(\vec{x})}{v_2(\vec{x})}\right]\left[\frac{v_1(\vec{x})}{u_{in}(\vec{x})}\right]\left[\frac{v_2(\vec{x})}{v_1(\vec{x})}\right] \tag{3}$$

in which $v_1(\vec{x})$ is the incident complex amplitude at the coating-air interface, while $v_2(\vec{x})$ is the reflected complex amplitude at that interface.

The first two phase factors on the right-hand side of Eq. (3) are gained by the light when traveling across the gap between the fixed reference plane (see Fig. 1) and the coating-air interface; we therefore obtain, up to a constant phase factor,

$$\left[\frac{u_{out}(\vec{x})}{v_2(\vec{x})}\right]\left[\frac{v_1(\vec{x})}{u_{in}(\vec{x})}\right] = e^{-2ik_0[\delta z_s(\vec{x}) + \Sigma_{j=1}^{N} \delta l_j(\vec{x})]} \tag{4}$$

where $k_0 = \omega_0/c$ is the wave number of the laser (ω_0 is its angular frequency) in vacuum, $\delta z_s(\vec{x})$ is the

vertical displacement of the coating-substrate interface (from its zero point), and $\delta l_j(\vec{x})$ is the thickness fluctuation of the jth coating layer—both evaluated at a transverse location $\vec{x}$.

The remaining complex reflectivity $v_2(\vec{x})/v_1(\vec{x})$ can be determined as a function of the phase shift experienced by the field in each layer, as well as the reflectivity of each interface, as described in detail in Sec. V. We can write

$$v_2/v_1 = \rho[\phi_1(\vec{x}), \ldots, \phi_N(\vec{x}); r_{01}(\vec{x}), \ldots, r_{Ns}(\vec{x})]. \quad (5)$$

Here ρ is the complex reflectivity of a multilayer coating, measured at the coating-air interface, which in turn depends on the optical thickness $\phi_j(\vec{x})$ of each layer ($j = 1, \ldots, N$) and the reflectivity $r_{p,p+1}(\vec{x}) \equiv r_p(\vec{x})$ of each interface ($p = 0, \ldots, N$, with $p = N + 1$ representing the substrate, and $p = 0$ the vacuum outside the coating). Assembling the above Eqs. (3)–(5), we obtain

$$\rho_{\rm tot}(\vec{x}) = e^{-2ik_0[\delta z_s(\vec{x}) + \Sigma_{j=1}^{N} \delta l_j(\vec{x})]} \rho[\{\phi_j(\vec{x})\}; \{r_p(\vec{x})\}]. \quad (6)$$

Brownian thermal forces lead to fluctuations in both the real and imaginary parts of this complex reflectivity. Fluctuations in the argument of the complex reflectivity phase modulate the outgoing light and directly produce sensing noise. Fluctuations in the magnitude, on the other hand, amplitude modulate the outgoing light, and produce a ponderomotive force noise.

B. Thermal phase and amplitude noise

Brownian thermal fluctuations in coating geometry and refractive index modify the complex reflectivity $\rho_{\rm tot}(\vec{x})$ defined in Eq. (6). The real and imaginary parts of

$$\delta \log \rho_{\rm tot}(\vec{x}) = \frac{\delta \rho_{\rm tot}(\vec{x})}{\rho_{\rm tot}(\vec{x})} \quad (7)$$

encode the amplitude/intensity and phase fluctuations of the reflected light at position $\vec{x}$ on the mirror surface. In particular, intensity fluctuation of the reflected light is given by

$$\frac{\delta I(\vec{x})}{I(\vec{x})} = 2\frac{\delta|\rho_{\rm tot}(\vec{x})|}{|\rho_{\rm tot}(\vec{x})|} = 2\,{\rm Re}[\delta \log \rho_{\rm tot}(\vec{x})] \quad (8)$$

while phase fluctuation is given by

$$\delta\phi(\vec{x}) = \delta \arg[\rho_{\rm tot}(\vec{x})] = {\rm Im}[\delta \log \rho_{\rm tot}(\vec{x})]. \quad (9)$$

In this way, if we further write

$$\xi(\vec{x}) - i\zeta(\vec{x}) = -\frac{i}{2k_0}\delta[\log \rho_{\rm tot}], \quad (10)$$

with both ξ and ζ as real-valued functions of $\vec{x}$, with the dimensionality of displacement, they will represent phase and amplitude noise, respectively. In particular, from Eq. (9), we have

$$\delta\phi(\vec{x}) = 2k_0\xi(\vec{x}). \quad (11)$$

Because we measure the mirror's position through the additional phase shift gained by the light after being reflected, through the relation $\Delta\phi = 2k_0\Delta x$, Eq. (11) indicates that $\xi(\vec{x})$ is the displacement noise due to phase fluctuations of the reflected light imposed by the coating.

The quantity ζ (which, like ξ, is a length) is connected to amplitude/intensity noise via

$$2k_0\zeta(\vec{x}) = {\rm Re}[\delta \log \rho_{\rm tot}] = \frac{\delta I(\vec{x})}{2I(\vec{x})}. \quad (12)$$

As we shall discuss in Sec. II E, ζ will cause a fluctuating force on the mirror, and can eventually be converted to a displacement noise via a dimensionless factor, although the effect will turn out to be small for gravitational-wave detectors.

Inserting the dependence of $\rho_{\rm tot}$ on ρ, l_j and z_s [cf. Eq. (6)], we obtain

$$\begin{aligned}\xi(\vec{x}) - i\zeta(\vec{x}) = &-\delta z_s(\vec{x}) - \sum_{l=1}^{N}\delta l_j(\vec{x}) \\ &- \sum_{j=1}^{N}\frac{i}{2k_0}\left[\frac{\partial \log\rho}{\partial\phi_j}.\delta\phi_j(\vec{x})\right] \\ &- \sum_{p=0}^{N}\frac{i}{2k_0}\left[\frac{\partial \log\rho}{\partial r_p}.\delta r_p(\vec{x})\right]. \end{aligned} \quad (13)$$

The first two terms are due to the motion of the coating-air interface at location $\vec{x}$ and thickness fluctuations of the layers, while the last two terms are due to light penetration into the coating layers (see Fig. 5). In particular, the third term is due to fluctuations in the total phase the light gains when propagating within the jth layer, while the fourth term is due to the (effective) reflectivity of the pth interface (with $p = 0$ indicating the coating-air interface), whose origin will be explained below.

C. Fluctuations $\delta\phi_j$ and δr_p

Light propagating within the coating layers is affected by the *photoelastic* effect, namely an *isothermal* fluctuation in $\delta n_j(\mathbf{x})$ (note here that $\mathbf{x}$ is a 3-D vector) due to fluctuating Brownian stresses exerted onto the coating materials. Assuming *isotropy* of the coating materials, we can write

$$\delta n_j(\mathbf{x}) = \beta_j^L S_{zz}(\mathbf{x}) + \beta_j^T[S_{xx}(\mathbf{x}) + S_{yy}(\mathbf{x})] \quad (14)$$

with

$$\beta_j^L \equiv \left(\frac{\partial n_j}{\partial \log l}\right)_{A_j}, \qquad \beta_j^T \equiv \left(\frac{\partial n_j}{\partial \log A}\right)_{l_j}. \quad (15)$$

Here L stands for longitudinal, and T stands for transverse, and the subscripts A_j and l_j indicate fixing transverse area and longitudinal length, respectively. We have also used the usual strain definition

$$S_{ij} \equiv \frac{1}{2}\left[\frac{\partial u_i}{\partial x_j} + \frac{\partial u_j}{\partial x_i}\right] \tag{16}$$

where $u_i(\mathbf{x})$, $i = 1, 2, 3$ are components of the displacement vector of the mass element at position $\mathbf{x}$. Refer to Appendix B for more details in defining the elasticity quantities, and Appendix A 1 for more details on the photoelastic effect.

We note that in Eq. (14) S_{zz} is the fractional increase in length (i.e., linear expansion) in the longitudinal direction, while $S_{xx} + S_{yy}$ is the fractional increase in the transverse area. According to Appendix A 4, we can ignore the second term representing area fluctuations in Eq. (14) when the beam spot size is much larger than the coating thickness. In this case, we write β_j in place for β_j^L, whose value can be expressed in terms of a particular component of the photoelastic tensor; see Eq. (A5).

As we discuss in Appendix A 2, the first term of Eq. (14) causes two effects for light propagating along each direction (i.e., $+z$ and $-z$): it adds an additional phase shift, and it backscatters a fraction of the light into the opposite direction. As we show in Appendix A 3 [cf. Eqs. (16)–(18)], these effects can be accounted for by modifying the phase shift $\delta\phi_j$ of each coating layer and changing the reflectivity δr_j of the interface, in the following manner:

$$\delta\phi_j = k_0\Big[(n_j + \beta_j)\delta l_j - \frac{1 - r_j^2}{2r_j}\beta_j \delta l_j^c + \frac{1 + r_{j-1}^2}{2r_{j-1}}\beta_{j-1}\delta l_{j-1}^c\Big], \tag{17}$$

$$\delta r_j = k_0 t_j^2 \beta_j \delta l_j^s. \tag{18}$$

Here we have defined

$$\delta l_j^c = -\int_0^{l_j} S_{zz}(z_{j+1} + z)\cos(2k_0 n_j z)dz \tag{19}$$

$$\delta l_j^s = -\int_0^{l_j} S_{zz}(z_{j+1} + z)\sin(2k_0 n_j z)dz \tag{20}$$

for $j \geq 1$, $\delta l_0^s = \delta l_0^c = 0$, and

$$z_j \equiv \sum_{n=j}^{N} l_n \tag{21}$$

marks the z coordinate of the top surface of the jth layer. We can also write

$$\delta l_j = \int_0^{l_j} S_{zz}(z_{j+1} + z)dz. \tag{22}$$

Note that

$$\text{total coating thickness} \equiv z_1 > z_2 > \cdots > z_{N+1} \equiv 0 \tag{23}$$

Note that δr_j, as well as the last two terms in $\delta\phi_j$ are due to backscattering, and have not been considered by previous authors.

Inserting Eqs. (17) and (18) into Eq. (13), we obtain

$$\xi(\vec{x}) - i\zeta(\vec{x}) = -z_s(\vec{x}) - \sum_{j=1}^{N}\int_{z_{j+1}}^{z_j}\left[1 + \frac{i\epsilon_j(z)}{2}\right]u_{zz}(\vec{x}, z)dz \tag{24}$$

where

$$\begin{aligned}\epsilon_j(z) = {} & (n_j + \beta_j)\frac{\partial \log\rho}{\partial\phi_j} \\ & - \beta_j\left[\frac{1 - r_j^2}{2r_j}\frac{\partial\log\rho}{\partial\phi_j} - \frac{1 + r_j^2}{2r_j}\frac{\partial\log\rho}{\partial\phi_{j+1}}\right] \\ & \times \cos[2k_0 n_j(z - z_j)] - t_j^2\beta_j\frac{\partial\log\rho}{\partial r_j} \\ & \times \sin[2k_0 n_j(z - z_{j+1})],\end{aligned} \tag{25}$$

a term that accounts for all effects associated with light penetration. Here we need to formally define

$$\frac{\partial\log\rho}{\partial\phi_{N+1}} = 0 \tag{26}$$

because ϕ_{N+1} does not really exist. Alternatively, we can also write formulas separately for ξ and ζ, using only real-valued quantities. For ξ, we have,

$$\begin{aligned}\xi(\vec{x}) = {} & -z_s(\vec{x}) - \sum_{j=1}^{N}[\mathcal{T}_j^{\xi}\delta l_j(\vec{x}) + \mathcal{T}_j^{\xi c}\delta l_j^c(\vec{x}) \\ & + \mathcal{T}_j^{\xi s}\delta l_j^s(\vec{x})],\end{aligned} \tag{27}$$

where

$$\mathcal{T}_j^{\xi} = 1 - \frac{n_j + \beta_j}{2}\,\mathrm{Im}\left(\frac{\partial\log\rho}{\partial\phi_j}\right) \tag{28}$$

$$\begin{aligned}\mathcal{T}_j^{\xi c} = {} & -\frac{\beta_j}{4}\,\mathrm{Im}\left(\frac{\partial\log\rho}{\partial\phi_j}\right)\left(\frac{1 - r_j^2}{r_j}\right) \\ & + \frac{\beta_j}{4}\,\mathrm{Im}\left(\frac{\partial\log\rho}{\partial\phi_{j+1}}\right)\left(\frac{1 + r_j^2}{r_j}\right)\end{aligned} \tag{29}$$

$$\mathcal{T}_j^{\xi s} = -\frac{\beta_j t_j^2}{2}\,\mathrm{Im}\left(\frac{\partial\log\rho}{\partial r_j}\right) \tag{30}$$

are transfer functions from the various δl's to the displacement-equivalent thermal noise (see Fig. 6). For ζ, we have

$$\zeta(\vec{x}) = \sum_{j=1}[\mathcal{T}_j^{\zeta}\delta l_j(\vec{x}) + \mathcal{T}_j^{\zeta c}\delta l_j^c(\vec{x}) + \mathcal{T}_j^{\zeta s}\delta l_j^s(\vec{x})] \tag{31}$$

where

$$\mathcal{T}_j^{\zeta} = \frac{n_j + \beta_j}{2}\,\mathrm{Re}\left(\frac{\partial \log \rho}{\partial \phi_j}\right) \tag{32}$$

$$\mathcal{T}_j^{\zeta c} = \frac{\beta_j}{4}\,\mathrm{Re}\left(\frac{\partial \log \rho}{\partial \phi_j}\right)\left(\frac{1 - r_j^2}{r_j}\right) - \frac{\beta_j}{4}\,\mathrm{Re}\left(\frac{\partial \log \rho}{\partial \phi_{j+1}}\right)\left(\frac{1 + r_j^2}{r_j}\right) \tag{33}$$

$$\mathcal{T}_j^{\zeta s} = \frac{\beta_j t_j^2}{2}\,\mathrm{Re}\left(\frac{\partial \log \rho}{\partial r_j}\right) \tag{34}$$

For an arbitrary stack of dielectrics, ζ is comparable to the part of ξ [cf. Eq. (25)] that involves light penetration into the layers. In practice, however, for highly reflective stacks, the real parts of $\partial \log \rho / \partial \phi_j$ and $\partial \log \rho / \partial r_j$ all turn out to be small, and therefore fluctuations in ζ (which correspond to amplitude fluctuations) should be much less than fluctuations in ξ (which corresponds to phase fluctuations).

D. Mode selection for phase noise

So far we have dealt with phase and amplitude noise as functions at each location $\vec{x}$ on the mirror surface. However, there is only one displacement noise that the light will sense. In this and the next subsection, we show how $\xi(\vec{x})$ and $\zeta(\vec{x})$ should be converted into measurement noise. In doing so, we recognize that only one spatial optical mode is injected on resonance in the optical cavity, and this mode has a complex amplitude of $u_0(\vec{x})$ at the mirror surface. Now suppose we have $u_{\mathrm{in}} = u_0(\vec{x})$ incident on the mirror surface; we will then have $u_{\mathrm{out}}(\vec{x}) = \rho_{\mathrm{tot}}(\vec{x}) u_0(\vec{x})$, which contains not only the resonant mode, but also other modes, which do not resonate in the cavity.

Let us select only the component of $u_{\mathrm{out}}(\vec{x})$ that is in the resonant spatial mode that is driven; then we have a complex reflectivity of

$$\bar{\rho} = \frac{\int u_0^*(\vec{x}) u_{\mathrm{out}}(\vec{x}) d^2\vec{x}}{\int u_0^* u_0 d\vec{x}} = \frac{\int \rho_{\mathrm{tot}}(\vec{x}) I(\vec{x}) d^2\vec{x}}{\int I(\vec{x}) d^2\vec{x}}, \tag{35}$$

specifically for the resonant mode, and hence independent of $\vec{x}$. Here we have defined $I(\vec{x}) \equiv |u_0(\vec{x})|^2$. Note that the bar on top of $\bar{\rho}$ represents averaging over the phase front, instead of averaging over time.

Now, inserting Eq. (10) as definitions for $\xi(\vec{x})$ and $\zeta(\vec{x})$ into Eq. (35), we obtain the fluctuating part of $\bar{\rho}$

$$\frac{\delta\bar{\rho}}{\bar{\rho}} = 2ik_0(\bar{\xi} - i\bar{\zeta}), \tag{36}$$

where

$$\bar{\xi} \equiv \frac{\int \xi(\vec{x}) I(\vec{x}) d^2\vec{x}}{\int I(\vec{x}) d^2\vec{x}}, \qquad \bar{\zeta} \equiv \frac{\int \zeta(\vec{x}) I(\vec{x}) d^2\vec{x}}{\int I(\vec{x}) d^2\vec{x}}. \tag{37}$$

Note that $2ik_0\bar{\xi}$ is the additional phase gained by the returning light, while $2k_0\bar{\zeta}$ is the relative change in amplitude [see discussions in Sec. II B]. Focusing first on $\bar{\xi}$, we note that this creates the same phase change as that gained by the reflected light if the mirror does not deform but instead is displaced along the beam by $\bar{\xi}$. In this way, $\bar{\xi}$ is an error in our measurement of the mirror's displacement.

E. Conversion of amplitude noise into displacement

The amplitude thermal noise can produce a spurious gravitational-wave signal by modulating the radiation pressure acting on the mirror, which in turn drives spurious mirror motion. Let us first consider a single-bounce scenario, in which an incoming beam with intensity profile $I(\vec{x})$, unaffected by thermal noise, is reflected with an intensity profile $I(\vec{x}) + \delta I(\vec{x})$, with $\delta I(\vec{x})$ induced by amplitude thermal noise. In this case, the mirror feels a thermal-noise-induced recoil force of

$$F_{\mathrm{th}}^{\mathrm{single}} = \int \frac{\delta I(\vec{x})}{c}\, d^2\vec{x}. \tag{38}$$

Using Eqs. (12) and (37), we obtain

$$F_{\mathrm{th}}^{\mathrm{single}} = \frac{4 I_0 k_0}{c}\,\bar{\zeta} \tag{39}$$

with I_0 the power incident on the mirror. If the mirror is within a cavity, then we need to consider both the increase in the circulating power (which we denote by I_c) with respect to the input power, and the coherent buildup of amplitude modulation within the cavity. We also note that now both the incident and reflected beam contains amplitude modulation, and that we must also consider the effect of this amplitude modulation on the input mirror.

If we restrict ourselves to a single optical cavity on resonance, then the thermal-noise force below the cavity bandwidth is given by

$$F_{\mathrm{th}}^{\mathrm{cav}} = \frac{16 k_0 I_c}{c\sqrt{T_{\mathrm{i}}}}\,\bar{\zeta}. \tag{40}$$

Here I_c is the circulating power in the arm cavity. Suppose both input and end mirrors have the same mass M; then the spectrum of cavity length modulation driven by the amplitude thermal noise at angular frequency Ω is given by

$$\sqrt{S_{\mathrm{th}}^{\mathrm{amp}}(\Omega)} = \frac{2}{M\Omega^2}\sqrt{S_{F_{\mathrm{th}}^{\mathrm{cav}}}} = \frac{32\omega_0 I_c}{m\Omega^2 c^2\sqrt{T_{\mathrm{i}}}}\sqrt{S_{\bar{\zeta}}}. \tag{41}$$

Note that $\bar{\zeta}$ has the units of displacement, and therefore the prefactor in front of $\sqrt{S_{\bar{\zeta}}}$ in Eq. (41) is a dimensionless conversion factor from $\bar{\zeta}$ to displacement noise. For Advanced LIGO, this cannot be completely dismissed at this stage, because

$$\frac{32\omega_0 I_c}{m\Omega^2 c^2\sqrt{T_{\mathrm{i}}}} = 18 \cdot \frac{I_c}{800\ \mathrm{kW}} \cdot \frac{40\ \mathrm{kg}}{m} \cdot \left[\frac{10\ \mathrm{Hz}}{\Omega/(2\pi)}\right]^2 \sqrt{\frac{0.03}{T_{\mathrm{i}}}}. \tag{42}$$

Nevertheless, as we will show in Sec. V B, the minor amplification factor here is not enough to make amplitude noise significant, because ζ is much less than ξ, for the coatings we consider.

III. THERMAL NOISE ASSUMING NO LIGHT PENETRATION INTO THE COATING

In this section, we compute the coating Brownian noise assuming that the incident light does not penetrate into the coating. This means light is promptly reflected at the coating-air interface, and therefore we should only keep the first two terms on the right-hand side of Eq. (13), which leads to $\zeta = 0$. We therefore consider only coating phase noise ξ, in particular its weighted average over the mirror surface, $\bar{\xi}$; see Eq. (37).

A. The fluctuation-dissipation theorem

The fluctuation-dissipation theorem relates the near-equilibrium thermal noise spectrum of a generalized coordinate q to the rate of dissipation in the system when a generalized force acts directly on this coordinate. More specifically, the thermal noise spectrum of q at temperature T is given by [13]

$$S_q(f) = \frac{k_B T}{\pi^2 f^2} \mathrm{Re}[Z(f)] \tag{43}$$

where f is frequency, $Z(f)$ is the mechanical impedance (inverse of admittance), or

$$Z(f) = -2\pi i f q(f)/F(f). \tag{44}$$

Alternatively, suppose we apply a sinusoidal force

$$F(t) = F_0 \cos(2\pi f t) \tag{45}$$

with amplitude F_0 acting directly on q; Eq. (43) can also be written as

$$S_x(f) = \frac{4k_B T}{\pi f} \frac{W_{\mathrm{diss}}}{F_0^2} = \frac{4k_B T}{\pi f} \frac{U}{F_0^2} \phi \tag{46}$$

where W_{diss} is the energy dissipated per cycle of oscillation divided by 2π (in other words, W_{diss} is the average energy loss per radian), U is the peak of the stored energy in the system, and ϕ is the loss angle, defined by

$$\phi = \mathrm{Re}[Z(f)]/\mathrm{Im}[Z(f)]. \tag{47}$$

It is important to note that ϕ is in general frequency dependent. However, for an elastic body, if the frequency is low enough (well below the first eigenfrequency), then U can be computed using the quasistatic approximation, because it is equal to the elastic energy stored in the equilibrium configuration when a constant force F_0 is applied to the system.

B. Mechanical energy dissipations in elastic media

It is straightforward to apply Eq. (46) to calculate the thermal noise component due to fluctuation of the position of the coating-air interface—the weighted average [cf. Eq. (35)] of the first two terms of Eq. (13). This can be obtained by applying a force F with a pressure profile proportional to $I(\vec{x})$ to the mirror surface (coating-air interface). In this case, elastic energy can be divided into bulk energy U_B and shear energy U_S (Chapter I of Ref. [18]), with

$$U_{\mathrm{coating}} = U_B + U_S = \int_{\mathrm{coating}} \left(\frac{K}{2} \Theta^2 + \mu \Sigma_{ij} \Sigma_{ij} \right) dV, \tag{48}$$

where Θ is the expansion, and Σ_{ij} is the shear tensor (see Appendix B for details). If we give small imaginary parts to K and μ, writing

$$\tilde{K} = K(1 + i\phi_B), \qquad \tilde{\mu} = \mu(1 + i\phi_S) \tag{49}$$

then W_{diss} can be written as

$$W_{\mathrm{diss}} = \phi_B U_B + \phi_S U_S. \tag{50}$$

Here we have introduced the loss angles ϕ_B and ϕ_S, which are associated with the dissipation of expansion energy density and the shear energy density, respectively. Note that our way of characterizing loss differs from previous work by Harry *et al.* [14], because for isotropic materials, ϕ_B and ϕ_S are the two fundamentally independent loss angles that characterize the dissipation of bulk and shear elastic energy; were we to literally adopt $\phi_\perp$ and $\phi_\parallel$ as done in Ref. [14], and consider them independent from each other, then the dissipated energy defined this way can turn out to be negative if certain force distributions are applied onto the mirror, which would be unphysical. See Appendix C for more details.

Once we have introduced ϕ_{B} and ϕ_{S}, other elastic moduli also gain small imaginary parts correspondingly. For example, for the most widely used Young's modulus and Poisson's ratio, because

$$K = \frac{Y}{3(1 - 2\sigma)}, \qquad \mu = \frac{Y}{2(1 + \sigma)} \tag{51}$$

we can write

$$\tilde{Y} = Y(1 + i\phi_Y) \tag{52}$$

with

$$\phi_Y = \frac{(1 - 2\sigma)\phi_B + 2(1 + \sigma)\phi_S}{3} \tag{53}$$

and

$$\tilde{\sigma} = \sigma + \frac{i}{3}(1 - 2\sigma)(1 + \sigma)(\phi_B - \phi_S). \tag{54}$$

Since $-1 < \sigma < 1/2$, we have $(1 - 2\sigma)(1 + \sigma) > 0$; therefore $\tilde{\sigma}$ has a positive imaginary part as ϕ_B is greater

than ϕ_S, and vice versa. To understand the physical meaning of the imaginary part of a Poisson's ratio, one has to realize that the Young's modulus and the Poisson's ratio together describe the elastic response of a rod. Suppose we apply an oscillatory tension uniformly along a rod at a very low frequency; whether the area of the rod leads or lags the length of the rod depends on the relative magnitudes of the bulk and shear loss angles. In the situation when the two loss angles ϕ_B and ϕ_S are equal to each other, the Poisson's ratio is real, and we only need to deal with one loss angle ϕ_Y—although there is reason to assume the equality of these two angles.

If the coating material is made into the shape of a one-dimensional rod, and if we only consider its elongational, bending or torsional modes, then the Young's modulus is the appropriate elastic modulus associated with these modes, and ϕ_Y is the appropriate loss angle to apply. However, this is not directly relevant for coating thermal noise. An elastic modulus that will actually prove useful is that of the *two-dimensional (2D) flexural rigidity* of a thin plate made from the coating material,

$$D = \frac{Yh}{12(1-\sigma^2)} = |D|(1 + i\phi_D) \tag{55}$$

where h is the thickness of the plate, with

$$\phi_D = \frac{(1-\sigma-2\sigma^2)\phi_B + 2(1-\sigma+\sigma^2)\phi_S}{3(1-\sigma)}. \tag{56}$$

As we shall see in Sec. VII A, this D is most easily measured through the quality factor of drum modes of a thinly coated sample—although this will not turn out to be the combination of loss angles that appear in the thermal noise of coated mirrors.

C. Thermal noise of a mirror coated with one thin layer

In the case where the coating thickness is much less than the size of the mirror substrate and the beam spot size, the elastic deformation of the substrate is not affected by the presence of the coating. As a consequence, if we include the elastic energy stored in the substrate $U_{\rm sub}$ with loss angle $\phi_{\rm sub}$, we can write

$$\begin{aligned} W_{\rm diss} &= \phi_{\rm sub}U_{\rm sub} + \phi_B U_B + \phi_S U_S \\ &\approx \left[\phi_{\rm sub} + \phi_B\frac{U_B}{U_{\rm sub}} + \phi_S\frac{U_S}{U_{\rm sub}}\right]U_{\rm sub}. \end{aligned} \tag{57}$$

With the assumption of a thin coating and a half-infinite substrate, the total strain energy stored in the sample can be considered as $U_{\rm sub}$. In such a way the coating adds on to the substrate loss angle as additional, effective angles

$$\phi_{\rm coated} = \phi_{\rm sub} + \frac{U_B}{U_{\rm sub}}\phi_B + \frac{U_S}{U_{\rm sub}}\phi_S. \tag{58}$$

Note that when the total coating thickness l is much less than the beam spot size w_0, we have $U_B/U_{\rm sub} \sim U_S/U_{\rm sub} \sim l/w_0 \ll 1$. Unfortunately, however, ϕ_B and ϕ_S are found to be so much larger than the substrate loss angle $\phi_{\rm sub}$ that in practice coating thermal noise still dominates over substrate thermal noise.

Now suppose we would like to measure a weighted average of the position of the mirror surface,

$$q = \bar{\xi} = \int d^2\vec{x}\, w(\vec{x}) z(\vec{x}) \tag{59}$$

with [cf. Eq. (37)]

$$w(\vec{x}) = \frac{I(\vec{x})}{\int I(\vec{x}) d^2\vec{x}} \tag{60}$$

and $z(\vec{x})$ the position of the coating-air interface at transverse location $\vec{x}$.

According to Sec. III A, we need to apply a pressure profile of

$$f(\vec{x}) = F_0 w(\vec{x}) \tag{61}$$

onto the upper surface of the coating, which we shall also refer to as the coating-air interface. Straightforward calculations give

$$\begin{aligned} \frac{U_B}{F_0^2} = \frac{(1-2\sigma_c)l}{3}\Bigg[&\frac{Y_c}{Y_s^2}\frac{(1-2\sigma_s)^2(1+\sigma_s)^2}{(1-\sigma_c)^2} \\ &+ \frac{1}{Y_s}\frac{2(1-2\sigma_s)(1+\sigma_s)(1+\sigma_c)}{(1-\sigma_c)^2} + \frac{1}{Y_c}\frac{(1+\sigma_c)^2}{(1-\sigma_c)^2}\Bigg] \\ &\times \int w^2(\vec{x}) d^2\vec{x} \end{aligned} \tag{62}$$

$$\begin{aligned} \frac{U_S}{F_0^2} = \frac{2l}{3}\Bigg[&\frac{Y_c}{Y_s^2}\frac{(1-\sigma_c+\sigma_c^2)(1+\sigma_s)^2(1-2\sigma_s)^2}{(1-\sigma_c)^2(1+\sigma_c)} \\ &- \frac{(1+\sigma_c)(1-2\sigma_c)(1-2\sigma_s)(1+\sigma_s)}{Y_s(1-\sigma_c)^2} \\ &+ \frac{(1-2\sigma_c)^2(1+\sigma_c)}{Y_c(1-\sigma_c)^2}\Bigg]\int w^2(\vec{x}) d^2\vec{x}. \end{aligned} \tag{63}$$

Here l is coating thickness; for Young's modulus Y and Poisson's ratio σ, substrates c and s represent coating and substrate, respectively. Directly following Eqs. (46) and (50) will give rise to a noise spectrum of

$$S_{\bar{\xi}} = \frac{4k_BT}{\pi f}\left[\phi_B\frac{U_B}{F_0^2} + \phi_S\frac{U_S}{F_0^2}\right] \tag{64}$$

where U_B/F_0^2 and U_S/F_0^2 are given by Eqs. (62) and (63) respectively.

Here we can define

$$\int w^2(\vec{x}) d^2\vec{x} = \frac{\int d^2\vec{x} I^2(\vec{x})}{[\int d^2\vec{x} I(\vec{x})]^2} \equiv \frac{1}{\mathcal{A}_{\rm eff}} \tag{65}$$

as the inverse of an *effective beam area*. Therefore noise power in q is proportional to coating thickness and inversely proportional to beam area. In particular, for a Gaussian beam with

$$I(\vec{x}) \propto \exp\left(-\frac{\vec{2}x^2}{w_0^2}\right) \tag{66}$$

the effective area is $\mathcal{A}_{\rm eff} = \pi w_0^2$.

Let us compare our results to previous calculations using $\phi_\perp$ and $\phi_\parallel$. As it turns out, if we assume $\phi_S = \phi_B$, then formulas for thermal noise agree with Eq. (22) in Ref. [14]. To illustrate the different roles now played by ϕ_B and ϕ_S, let us take the very simple case of $Y = Y_c = Y_s$ and $\sigma = \sigma_c = \sigma_s$, where

$$\frac{\delta U_B}{F_0^2} = \frac{4l}{3Y\mathcal{A}_{\rm eff}}(1+\sigma)^2(1-2\sigma) \tag{67}$$

$$\frac{\delta U_S}{F_0^2} = \frac{2l}{3Y\mathcal{A}_{\rm eff}}(1+\sigma)(1-2\sigma)^2. \tag{68}$$

Using Eq. (64), we can get the power spectral density of the single-layer nonpenetration coating thermal noise as

$$S_{\bar{\xi}}(f) = \frac{8k_BT(1-\sigma-2\sigma^2)l}{3\pi fY\mathcal{A}_{\rm eff}}[2(1+\sigma)\phi_B + (1-2\sigma)\phi_S]. \tag{69}$$

From Eq. (69), we can see that the bulk loss and shear loss contribute differently to the total noise. More importantly, at least in the simple case where $Y_c = Y_s$, the combination of ϕ_B and ϕ_S is approximately $2\phi_B + \phi_S$, which differs significantly from the combination $\phi_{\rm tot} \approx \phi_B + 2\phi_S$ measured by the ring-down experiments that have been performed so far [19–21]. This will be discussed in detail in the rest of Sec. VII.

D. Discussions on the correlation structure of thermal noise

Before proceeding to more detailed calculations of Brownian noise that involve light penetrating into the coating layers, we would like to gain more insight about thermal noise by inspecting our existing expressions of coating thermal noise [Eqs. (62)–(64)] more carefully. We note that

$$S_{\bar{\xi}} \propto l\int w^2(\vec{x})d^2\vec{x}, \tag{70}$$

where the coefficient of proportionality depends only on material property. From such a dependence on coating and beam geometries, we deduce that (i) each point on the coating-air interface fluctuates along the z direction independently, and (ii) materials at different z's within the coating also contribute independently to coating thermal noise. These observations will be confirmed below in Sec. IV.

Finally, within the coefficient of proportionality [cf. Eqs. (62) and (63)], we found three types of dependence on the Young's moduli of the coating and substrate materials: terms proportional to $1/Y_c$ are expected to arise from fluctuations in coating thickness, terms proportional to Y_c/Y_s^2 can be interpreted as arising from coating thermal stresses driving the substrate-coating interface, while terms proportional to $1/Y_s$ are therefore interpreted as correlations between the above two types of noise.

IV. CROSS SPECTRA OF THERMAL NOISE COMPONENTS

In this section, we compute the cross spectra of each component of coating thermal noise, and assemble the formula for the spectral density of the total noise. Specifically, in Sec. IV A, we compute the cross spectra of the thickness fluctuations between any two uniform sublayers of the coating, and obtain the cross spectrum of S_{zz}; in Sec. IV B, we compute the cross spectra involving height fluctuation z_s of the coating-substrate interface, i.e., $S_{S_{zz}z_s}$ and $S_{z_sz_s}$; in Sec. IV C, we dissect the above results and analyze the separate roles of bulk and shear fluctuations; in Sec. IV D, we write down the full formula for coating thermal noise.

A. Coating-thickness fluctuations

Let us start by calculating thickness fluctuations of individual layers and correlations between them. Following Levin's approach, we imagine applying two pairs of opposite pressure,

$$f_1(\vec{x}) = F_0 w_1(\vec{x}), \qquad f_3(\vec{x}) = F_0 w_3(\vec{x}) \tag{71}$$

in the z direction on layer I and layer III, as shown in Fig. 2, with thicknesses of l_1 and l_3, respectively. Here $w_1(\vec{x})$ and $w_3(\vec{x})$, like the $w(\vec{x})$ used in Eq. (59), provide the shape of the pressure profiles. Note that we apply pairs of forces, and each pair must be equal and opposite in direction because we are interested in learning about the fluctuations of the *thickness*, instead of the location, of the layers.

We assume that layers I and III are each made from a single type of material, yet there could be an arbitrary number of different material sublayers in II. As it will turn out, the precise locations of layers I and III along the z direction do not affect the result, *as long as they do not overlap*, or in other words, layer II has nonzero thickness.

Throughout this paper, we shall assume that the beam spot size is much less than the radius of the mirror, so that we can make the approximation that the mirror surface is an infinite two-dimensional plane. In this case, we perform a spatial Fourier transformation for the applied pressure,

$$\tilde{f}_j(\vec{k}) = \int e^{i\vec{k}\cdot\vec{x}} f_j(\vec{x})d^2\vec{x} = F_0\tilde{w}_j(\vec{k}), \qquad j = 1, 3, \tag{72}$$

and carry out our calculations for strain and stress distributions in the coating-substrate system in the Fourier domain.

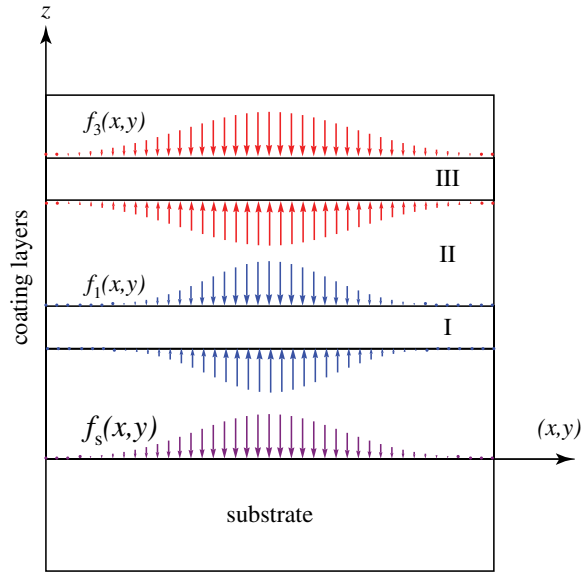

FIG. 2 (color online). Illustrations of forces applied onto various interfaces within the coating. Each of layers I and III in the coating are assumed to be uniform (but they might each contain a different kind of material); region II denotes the entire gap between them, which may well contain many different dielectric layers. A pair of force distributions f_1 (f_3) with the same pressure profile but in opposite directions is exerted on opposite sides of layer I (III), while f_s is exerted on the coating-substrate interface. (Although each pair has the same pressure profile, they may be different from each other.) The three distributions may well have different profiles (as also illustrated in the figure).

We further assume that the coating thickness is much less than the beam spot size, which is inverse to the maximum spatial frequency contained in $\tilde{w}_{1,3}$. This means we only need to consider $\vec{k}$'s with $|\vec{k}|l \ll 1$, with l the total coating thickness. According to calculations in Appendix B, nonzero components of the stress and strain tensors in layers I and III are found to be (in the spatial Fourier domain)

$$\tilde{T}^{\mathrm{I}}_{xx} = \tilde{T}^{\mathrm{I}}_{yy} = \frac{\sigma_1 \tilde{w}_1}{1-\sigma_1} F_0, \qquad \tilde{T}^{\mathrm{I}}_{zz} = \tilde{w}_1 F_0, \tag{73}$$

$$\tilde{S}^{\mathrm{I}}_{zz} = -\frac{(1-2\sigma_1)(1+\sigma_1)\tilde{w}_1}{Y_1(1-\sigma_1)} F_0, \tag{74}$$

and

$$\tilde{T}^{\mathrm{III}}_{xx} = \tilde{T}^{\mathrm{III}}_{yy} = \frac{\sigma_3 \tilde{w}_3}{1-\sigma_3} F_0, \qquad \tilde{T}^{\mathrm{III}}_{zz} = \tilde{w}_3 F_0, \tag{75}$$

$$\tilde{S}^{\mathrm{III}}_{zz} = -\frac{(1-2\sigma_3)(1+\sigma_3)\tilde{w}_3}{Y_3(1-\sigma_3)} F_0, \tag{76}$$

respectively.

Note that deformations within layer I only depend on $\tilde{w}_1$ (not $\tilde{w}_3$), while deformations within layer III only depend on $\tilde{w}_3$ (not $\tilde{w}_1$)—while regions outside these layers are found to have vanishing strain and stress. This means we can treat deformations caused by each pair of forces independently, as long as layer I and layer III do not overlap. The deformations are also independent of the thickness of the layers. The vanishing of deformations outside these layers means that when we introduce additional pairs of opposite forces, the new deformations introduced will be constrained within those new layers—as long as those new layers do not overlap with existing ones. This independence originates from the linearity of elastic response, and the fact that coating strains induced by force applied on a single surface within the coating, as discussed in Appendix B, do not depend on distance away from that surface, as seen in Eqs. (25)–(32). The situation here is analogous to the electrostatics of several pairs of oppositely charged infinite parallel planes.

In terms of thermal noise, such a distribution of elastic deformations corresponds to a dissipation energy that consists of two independent terms, each corresponding to one layer and proportional to its thickness:

$$\frac{W_{\mathrm{diss}}}{F_0^2} = W_{11} l_1 \int w_1^2 d^2\vec{x} + W_{33} l_3 \int w_3^2 d^2\vec{x}. \tag{77}$$

Here we have defined, for $j = 1, 3$,

$$W_{jj} \equiv \frac{(1-2\sigma_j)(1+\sigma_j)}{3(1-\sigma_j)^2 Y_j}\left[\frac{1+\sigma_j}{2}\phi_B^j + (1-2\sigma_j)\phi_S^j\right]. \tag{78}$$

This means the fluctuation of

$$q \equiv \int [w_1(\vec{x})\delta l_1(\vec{x}) + w_3(\vec{x})\delta l_3(\vec{x})] d^2\vec{x} \tag{79}$$

is given by

$$S_q = \frac{4k_B T}{\pi f} \sum_{j=1,3}\left[W_{jj} l_j \int w_j^2(\vec{x}) d^2\vec{x}\right]. \tag{80}$$

The absence of a cross term between w_1 and w_3 means that fluctuations in $\delta l_1(\vec{x})$ and $\delta l_3(\vec{x}')$ are uncorrelated—and hence statistically independent. Furthermore, within each layer, in the same spirit as the discussions in Sec. III D, the particular form of dependence on l_j and $w_j(\vec{x})$ indicates that S_{zz} fluctuations at different 3-D locations (within this layer) are all uncorrelated and have the same spectrum. In this way, we obtain the cross spectral density of S_{zz} at two arbitrary 3-D locations within the coating:

$$S^{ij}_{S_{zz}S_{zz}}(\vec{x}, z; \vec{x}', z') = \frac{4k_B T}{\pi f}\delta_{ij}\delta^{(2)}(\vec{x}-\vec{x}')\delta(z-z')W_{jj}. \tag{81}$$

Here we have assumed that $(\vec{x}, z)$ belongs to layer i, while $(\vec{x}', z')$ belongs to layer j. (The association to layers helps to identify the material property to be used in W_{jj}.)

B. Fluctuations of coating-substrate interface and their correlations with coating thickness

To investigate the correlation between the height of the coating-substrate interface, $z_s(\vec{x})$, and the thickness of each coating layer, $\delta l_j(\vec{x})$, we apply an identical pair of pressures $f_1(\vec{x}) = F_0 w_1(\vec{x})$ at opposite sides of layer I, and force $f_s(x, y) = F_0 w_s(\vec{x})$ onto the coating-substrate interface (along the $-z$ direction), as shown in Fig. 1. The same strain and stress as in Eqs. (73) and (74) are driven by $\tilde{f}_1$, which are only nonvanishing within layer I. On the other hand, $\tilde{f}_s$ drives uniform strain and stress over the entire coating, with nonvanishing components of stress and strain given by

$$\| \tilde{T}_{ij} \| = \frac{\tilde{w}_s(1-\sigma_s-2\sigma_s^2)Y_c}{(1+\sigma_c)\kappa^2 Y_s}\begin{bmatrix} \frac{k_x^2+\sigma_c k_y^2}{1-\sigma_c} & k_x k_y & 0 \\ k_x k_y & \frac{\sigma_c k_x^2+k_y^2}{1-\sigma_c} & 0 \\ 0 & 0 & 0 \end{bmatrix} \tag{82}$$

$$\| \tilde{S}_{ij} \| = -\frac{\tilde{w}_s(1-\sigma_s-2\sigma_s^2)}{\kappa^2 Y_s}\begin{bmatrix} k_x^2 & k_x k_y & 0 \\ k_x k_y & k_y^2 & 0 \\ 0 & 0 & \frac{-\sigma_c}{1-\sigma_c} \end{bmatrix}, \tag{83}$$

where Young's modulus Y_c and Poisson's ratio σ_c of the coating are given by values within layer I. The total dissipation in this case will have the following structure:

$$\frac{W_{\rm diss}}{F_0^2} = l_1\Big[W_{11}\int w_1^2 d^2\vec{x} + 2W_{1s}\int w_1 w_s d\vec{x} + W_{ss}\int w_s^2 d^2\vec{x}\Big], \tag{84}$$

with the first term arising from dissipation in layer I that is due to strain and stress driven by f_1; the second term also arising from dissipation in layer I due to cross terms between strains and stresses caused by f_1 and f_s; and the third term arising from dissipations throughout the entire coating, due to strain and stress caused by f_s. Here W_{11} is the same as defined by Eq. (78), and

$$W_{js} = \frac{(1-\sigma_s-2\sigma_s^2)(1-\sigma_j-2\sigma_j^2)}{2(1-\sigma_j)^2 Y_s}(\phi_B^j - \phi_S^j) \tag{85a}$$

$$W_{ss}^{(j)} = \frac{(1-\sigma_s-2\sigma_s^2)^2 Y_j}{(1-\sigma_j)^2 Y_s^2}\Big[\frac{1-2\sigma_j}{2}\phi_B^j + \frac{1-\sigma_j+\sigma_j^2}{1+\sigma_j}\phi_S^j\Big]. \tag{85b}$$

Note that we have added a superscript (j) for W_{ss} to indicate that here the dissipation is due to the pair of forces applied on one thin layer alone.

Here again, the dependences on w_1^2 and w_s^2 indicate that fluctuations at different transverse locations, $\vec{x} \neq \vec{x}'$, are uncorrelated, while the l_1 in front of W_{11} and the arbitrariness of l_1 mean that S_{zz} fluctuations at different z locations within the thin layers are uncorrelated. The l_1 in front of both W_{1s} and W_{ss} indicates that all S_{zz} within layer I are correlated with z_s the same way, even though all of them are mutually uncorrelated.

This allows us to extract the following:

$$S_{z_s z_s}(\vec{x}, \vec{x}') = \frac{4k_B T}{3\pi f}\delta^{(2)}(\vec{x}-\vec{x}')\sum_j l_j W_{ss}^{(j)} \tag{86a}$$

$$S_{S_{zz}s_z}(\vec{x}; \vec{x}', z') = \frac{4k_B T}{3\pi f}\delta^2(\vec{x}-\vec{x}')W_{js}. \tag{86b}$$

Here for Eq. (86b), j is the layer with which z' is associated, and this labeling is to help identify which material parameter to use in W_{js}.

C. The anatomy of coating thermal noise

Here let us assemble Eqs. (81), (86a), and (86b), from the previous sections, and write

$$S^{ij}_{S_{zz}S_{zz}}(\vec{x}, z; \vec{x}', z') = \frac{4k_B T}{3\pi f}\frac{(1+\sigma_j)(1-2\sigma_j)}{Y_j(1-\sigma_j)^2}\Big[\frac{1+\sigma_j}{2}\phi_{Bj} + (1-2\sigma_j)\phi_{Sj}\Big]\delta_{ij}\delta^{(2)}(\vec{x}-\vec{x}')\delta(z-z') \tag{87a}$$

$$S_{z_s z_s}(\vec{x}, \vec{x}') = \frac{4k_B T}{3\pi f}\frac{(1-\sigma_s-2\sigma_s^2)^2}{Y_s^2}\sum_j \frac{Y_j l_j}{(1-\sigma_j)^2}\Big[\frac{1-2\sigma_j}{2}\phi_{Bj} + \frac{1-\sigma_j+\sigma_j^2}{1+\sigma_i}\phi_{Sj}\Big]\delta^{(2)}(\vec{x}-\vec{x}') \tag{87b}$$

$$S_{z_s S_{zz}}(\vec{x}; \vec{x}', z') = \frac{2k_B T}{3\pi f}\frac{(1-\sigma_s-2\sigma_s^2)(1-\sigma_j-2\sigma_i^2)}{Y_s(1-\sigma_j)^2}[\phi_{Bj} - \phi_{Sj}]\delta^2(\vec{x}-\vec{x}'). \tag{87c}$$

Here we have assumed that z belongs to the ith layer and that z' belongs to the jth layer, respectively. The thickness fluctuations of different layers are mutually independent [note the Kronecker delta in Eq. (87a)], while the thickness fluctuation of each layer is correlated with the height fluctuation of the coating-substrate interface [Eq. (87c)].

Fluctuations in the strain S_{zz} and the coating-substrate interface z_s, described by Eqs. (87a) and (87b), can be represented alternatively as being driven by a number of independent fluctuating fields that exist throughout the coating. Such a representation allows us to better appreciate the origin and the magnitude of these fluctuations.

In order to do so, let us first define $3N$ thermal noise fields (i.e., 3 for each coating layer), $n_j^B(\mathbf{x})$, $n_j^{S_A}(\mathbf{x})$ and $n_j^{S_B}(\mathbf{x})$, all independent from one another, with

$$S_{n_j^B n_k^B} = \frac{4k_B T(1-\sigma_j-2\sigma_j^2)}{3\pi f Y_j(1-\sigma_j)^2}\phi_B^j \delta_{jk}\delta^{(3)}(\mathbf{x}-\mathbf{x}'), \tag{88a}$$

$$S_{n_j^{S_A} n_k^{S_A}} = S_{n_j^{S_B} n_k^{S_B}} = \frac{4k_B T(1-\sigma_j-2\sigma_j^2)}{3\pi f Y_j(1-\sigma_j)^2}\phi_S^j \delta_{jk}\delta^{(3)}(\mathbf{x}-\mathbf{x}'), \tag{88b}$$

and all other cross spectra vanishing. Here j labels the coating layer, the superscript B indicates bulk fluctuation, while S_A and S_B label two types of shear fluctuations. The normalizations of these fields are chosen such that each of these fields, when integrated over a length l_j along z, has a noise spectrum that is roughly the same magnitude as a single-layer thermal noise.

Noise fields $n_j^B(\mathbf{x})$, $n_j^{S_A}(\mathbf{x})$ and $n_j^{S_B}$ can be used to generate thickness fluctuations of the layers and the interface fluctuation (87a) and (87b) if we define

$$u_{zz}(\vec{x}, z) = C_j^B n_j^B(\vec{x}, z) + C_j^{S_A} n_j^{S_A}(\vec{x}, z) \tag{89}$$

and

$$z_s(\vec{x}) = \sum_j \int_{L_{j+1}}^{L_j} dz[D_j^B n_j^B(\vec{x}, z) + D_j^{S_A} n_j^{S_A}(\vec{x}, z) + D_j^{S_B} n_j^{S_B}(\vec{x}, z)]. \tag{90}$$

For each coating layer, C_j^B and D_j^B are transfer functions from the bulk noise field n_j^B to its own thickness δl_j and to surface height z_s, respectively; $C_j^{S_A}$ and $D_j^{S_A}$ are transfer functions from the first type of shear noise to thickness and surface height; finally $D_j^{S_B}$ is the transfer function from the second type of shear noise to surface height (note that this noise field does not affect layer thickness). Explicit forms of these transfer functions are listed in Table I.

Equations (89) and (90) owe their simple forms to the underlying physics of thermal fluctuations.

For *bulk noise*, i.e., terms involving n_j^B, the form of Eqs. (89) and (90) indicates that the interface fluctuation due to bulk dissipation is simply a sum of pieces that are directly proportional to the bulk-induced thickness fluctuations of each layer. This means the thermal bulk stress in a layer drives simultaneously the thickness fluctuation of that layer and a fluctuation of the coating-substrate interface. The fact that D_j^B and C_j^B have the same sign means that when thickness increases, the interface also rises (with an intuitive explanation shown in Fig. 3). This sign of correlation is generally unfavorable because the two noises add constructively towards the rise of the coating-air interface.

For *shear noise*, the situation is a little more complicated, because unlike bulk deformations, there are a total of five possible shear modes. From Eqs. (73) and (74), it is clear that f_1, applied on opposites of layer I (Fig. 2), only drives the $xx + yy - 2zz$ shear mode and the $xx + yy + zz$ bulk mode, while from Eqs. (82) and (83), the force distribution f_s drives three shear modes of $xx - yy$, $xy + yx$, and $xx + yy - 2zz$. This means that while thermal shear stresses in the $xx + yy - 2zz$ mode drive layer thickness and interface fluctuation simultaneously, there are additional modes of shear stress, $xx - yy$ and $xy + yx$, that only drive the interface without driving layer thickness. Our mode S_A, which drives both layer thickness and interface height, therefore corresponds to the physical shear mode of $xx + yy - 2zz$; our mode S_B, which only drives interface height, corresponds to the joint effect of the physical shear modes $xx - yy$ and $xy + yx$. It is interesting to note that for S_A, its contributions to δl_j and z_s are anticorrelated, because C^{S_A} and D^{S_A} have opposite signs. This is intuitively explained in Fig. 3.

As an example application of Eqs. (89) and (90), if we ignore light penetration into the coating layers, namely, when thermal noise is equal to

TABLE I. Transfer functions from bulk and shear noise fields to layer thickness and surface height.

	Thickness (δ_j)	Surface height (z_s)
Bulk	$C_j^B = \sqrt{\frac{1+\sigma_j}{2}}$	$D_j^B = \frac{1-\sigma_s-2\sigma_s^2}{\sqrt{2(1+\sigma_j)}}\frac{Y_j}{Y_s}$
Shear A	$C_j^{S_A} = \sqrt{1-2\sigma_j}$	$D_j^{S_A} = -\frac{1-\sigma_s-2\sigma_s^2}{2\sqrt{1-2\sigma_j}}\frac{Y_j}{Y_s}$
Shear B	(none)	$D_j^{S_B} = \frac{\sqrt{3}(1-\sigma_j)(1-\sigma_s-2\sigma_s^2)}{2\sqrt{1-2\sigma_j}(1+\sigma_j)}\frac{Y_j}{Y_s}$

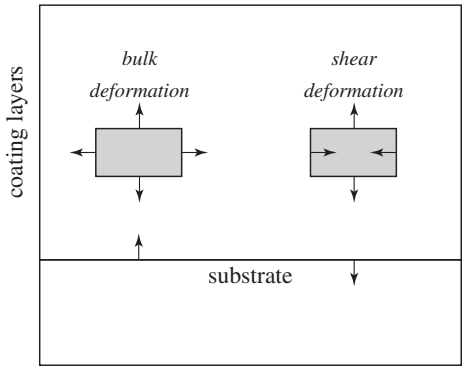

FIG. 3. Illustration of the correlations between coating thickness δl_j and the height of the coating-substrate interface, z_s. On the left, for a bulk deformation: When a coating element is expanding, its expansion along the x-y plane lifts the coating-substrate interface upwards, causing additional motion of the coating-air interface correlated to that caused by the increase in coating thickness. On the right, a particular shear mode: When a coating element is expanding, its contraction along the x-y plane pushes the coating-substrate interface downwards, causing additional motion of the coating-air interface anticorrelated to that caused by the increase in coating thickness.

$$\xi^{\rm np} \equiv -z_s - \sum_j \delta l_j \tag{91}$$

we have

$$\xi^{\rm np} = -\sum_j \int_{L_j}^{L_{j+1}} dz[(C_j^B + D_j^B)n_j^B + (C_j^{S_A} + D_j^{S_A})n_j^{S_A} + D_j^{S_B} n_j^{S_B}] \tag{92}$$

in which contributions from each layer have been divided into three mutually uncorrelated groups, each arising from a different type of fluctuation. Here we see explicitly that C^B and D^B sharing the same sign increases contributions from n^B; C^{S_A} and D^{S_A} having opposite signs suppresses contributions from n^{S_A}.

Finally, we note that in the spectral density of $\xi^{\rm np}$, contributions directly from coating thickness will be proportional to $|C_j^B|^2$ and $|C_j^{S_A}|^2$, and hence proportional to $1/Y_c$; those from interface height will be $|D_j^B|^2$, $|D_j^{S_A}|^2$ and $|D_j^{S_B}|^2$, and hence proportional to Y_c/Y_s^2; while those from correlations will be proportional to $C_j^B D_j^B$ and $C_j^{S_A} D_j^{S_A}$, and hence proportional to $1/Y_s$. This confirms our anticipation at the end of Sec. III D.

D. Full formula for thermal noise

Now we give the complete formulas for amplitude and phase noise spectrum [cf. Eq. (94) and (95)]. As we consider light penetration into the coating, we resort to Eq. (24), and write

$$\xi(\vec{x}) - i\zeta(\vec{x}) = -\sum_j \int_{z_{j+1}}^{z_j} dz\Big\{\Big[\Big[1 + \frac{i\epsilon_j(z)}{2}\Big]C_j^B + D_j^B\Big] \times n_j^B(\vec{x}, z) + \Big[\Big[1 + \frac{i\epsilon_j(z)}{2}\Big]C_j^{S_A} + D_j^{S_A}\Big] \times n_j^{S_A}(\vec{x}, z) + D_j^{S_B} n_j^{S_B}(\vec{x}, z)\Big]\Big\}. \tag{93}$$

Here spectra of independent fields n_j^B, $n_j^{S_A}$ and $n_j^{S_B}$ have been given in Eqs. (88a) and (88b), ϵ is defined in Eq. (25), while the transfer functions C and D are listed in Table I.

We can then obtain the spectrum of phase noise (after averaging over the mirror surface and weighted by the power profile of the optical mode) as

$$S_{\bar{\xi}} = \sum_j \int_{z_{j+1}}^{z_j} \frac{dz}{\lambda_j}\Big[\Big[1 - {\rm Im}\frac{\epsilon_j(z)}{2}\Big]C_j^B + D_j^B\Big]^2 S_j^B + \sum_j \int_{z_{j+1}}^{z_j} \frac{dz}{\lambda_j}\Big[\Big[1 - {\rm Im}\frac{\epsilon_j(z)}{2}\Big]C_j^{S_A} + D_j^{S_A}\Big]^2 S_j^S + \sum_j [D_j^{S_B}]^2 \frac{l_j}{\lambda_j} S_j^S \equiv \sum_j q_j^B S_j^B + q_j^S S_j^S \tag{94}$$

and the spectrum of amplitude noise as

$$S_{\bar{\zeta}} = \sum_j \int_{z_{j+1}}^{z_j} \frac{dz}{\lambda_j}\Big\{\Big[C_j^B\,{\rm Re}\frac{\epsilon_j(z)}{2}\Big]^2 S_j^B + \Big[C_j^{S_A}\,{\rm Re}\frac{\epsilon_j(z)}{2}\Big]^2 S_j^S\Big\}. \tag{95}$$

Here λ_j is the wavelength of light in layer j, and we have defined

$$S_j^X \equiv \frac{4k_B T \lambda_j \phi_X^j (1 - \sigma_j - 2\sigma_j^2)}{3\pi f Y_j (1 - \sigma_j)^2 \mathcal{A}_{\rm eff}}, \qquad X = B, S, \tag{96}$$

which is at the level of coating thickness fluctuation of a single layer of dielectrics with material parameters identical to layer j and length equal to λ_j. Note that the quantity S_j^X only depends on the material properties (and temperature) of the layer, and is independent from the length of that layer; the quantities q_j^X (see Fig. 7), on the other hand, give us the relative thermal noise contribution of each layer in a dimensionless way.

Note that the reason for keeping the integrals in Eqs. (94) and (95) is because ϵ has a z dependence, which originates from the fact that the backscattering contributions to $\delta\phi_j$ and δr_j are a weighted integral of u_{zz} within each layer [cf. (17) and (18)].

V. EFFECT OF LIGHT PENETRATION INTO THE COATING

In this section, we synthesize results from Sec. II and IV, and compute the full Brownian thermal noise for coating configurations. We will illustrate how the light penetration affects the total noise in highly reflective coatings.

A. Optics of multilayer coatings

For the completeness of the paper, we briefly review how the light penetration coefficient $\partial \log\rho/\partial\phi_j$ can be calculated.

From an interface from layer i to j (here j is either $i+1$ or $i-1$), we denote the reflectivity and transmissivity of different layers by r_{ij} and t_{ij}: $r_{ij}^2 + t_{ij}^2 = 1$,

$$r_{ij} = \frac{n_i - n_j}{n_i + n_j}. \tag{97}$$

We also define $n_{N+1} = n_1$, since that is the refractive index of the substrate.

A matrix approach can be applied to solve for the amplitude of light inside the layers, when we view the coating as made up of two elementary transformations, each representable by a matrix. In this approach, instead of writing outgoing fields in terms of ingoing fields, one writes fields to the right of an optical element in terms of those to the left. As illustrated in Fig. 4, for reflection at an interface (left panel), we write

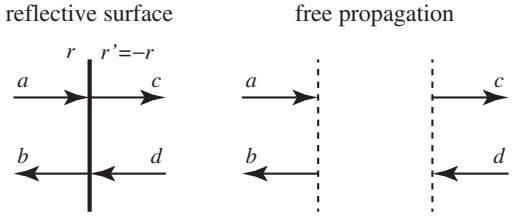

FIG. 4. Two basic transformations involved in solving for optical fields in a multilayer coating.

$$\begin{bmatrix} c \\ d \end{bmatrix} \equiv \mathbf{R}_r = \frac{1}{t}\begin{bmatrix} 1 & -r \\ -r & 1 \end{bmatrix}\begin{bmatrix} a \\ b \end{bmatrix}. \tag{98}$$

On the other hand, for propagation across a gap with phase shift ϕ, we have

$$\begin{bmatrix} c \\ d \end{bmatrix} \equiv \mathbf{T}_\phi = \begin{bmatrix} e^{i\phi} & 0 \\ 0 & e^{-i\phi} \end{bmatrix}\begin{bmatrix} a \\ b \end{bmatrix}. \tag{99}$$

In this way, assuming the input and output field amplitude at the top surface of a multilayer coating to be v_1 and v_2, and writing those right inside the substrate to be s_1 and s_2, we have

$$\begin{bmatrix} s_1 \\ s_2 \end{bmatrix} = \begin{bmatrix} M_{11} & M_{12} \\ M_{21} & M_{21} \end{bmatrix}\begin{bmatrix} v_1 \\ v_2 \end{bmatrix} = \mathbf{M}\begin{bmatrix} v_1 \\ v_2 \end{bmatrix} \tag{100}$$

where $\mathbf{M}$ is given by

$$\mathbf{M} = \mathbf{R}_{r_{N,N+1}}\mathbf{T}_{\phi_{N-1}}\mathbf{R}_{r_{N-1,N}}\ldots\mathbf{R}_{r_{12}}\mathbf{T}_{\phi_1}\mathbf{R}_{r_{01}}. \tag{101}$$

The complex reflectivity is given by

$$\rho = -M_{21}/M_{22}. \tag{102}$$

B. Levels of light penetration in Advanced LIGO End Test-Mass Mirror Coatings

In Advanced LIGO, the coating stack is made from alternating layers of two materials: SiO_2 ($n_1 = 1.45$) and Ta_2O_5 ($n_2 = 2.07$). Here we consider the end test-mass mirror (ETM). In order to achieve very high reflectivity, the coating is made of 19 successive pairs of alternating SiO_2 and Ta_2O_5 layers, all $\lambda/4$ in thickness except the top one, which is $\lambda/2$. We will refer to this as the *conventional coating*. An alternative design has been made to allow the coating to operate at both 1064 nm and 532 nm. We shall refer to this as the *Advanced LIGO coating* (see Appendix D) [22].

In Fig. 5, we plot real and imaginary parts of $\partial \log\rho/\partial\phi_j$ and $\partial \log\rho/\partial r_j$ [see Eq. (13)], for both conventional and Advanced LIGO coatings. Here we note that the real parts of these derivatives are of the order of 10^{-6}, which means $\bar{\zeta}$ is less than $\bar{\xi}$ by 6 orders of magnitude. This, together with considerations in Sec. II E, will make amplitude coating noise negligible.

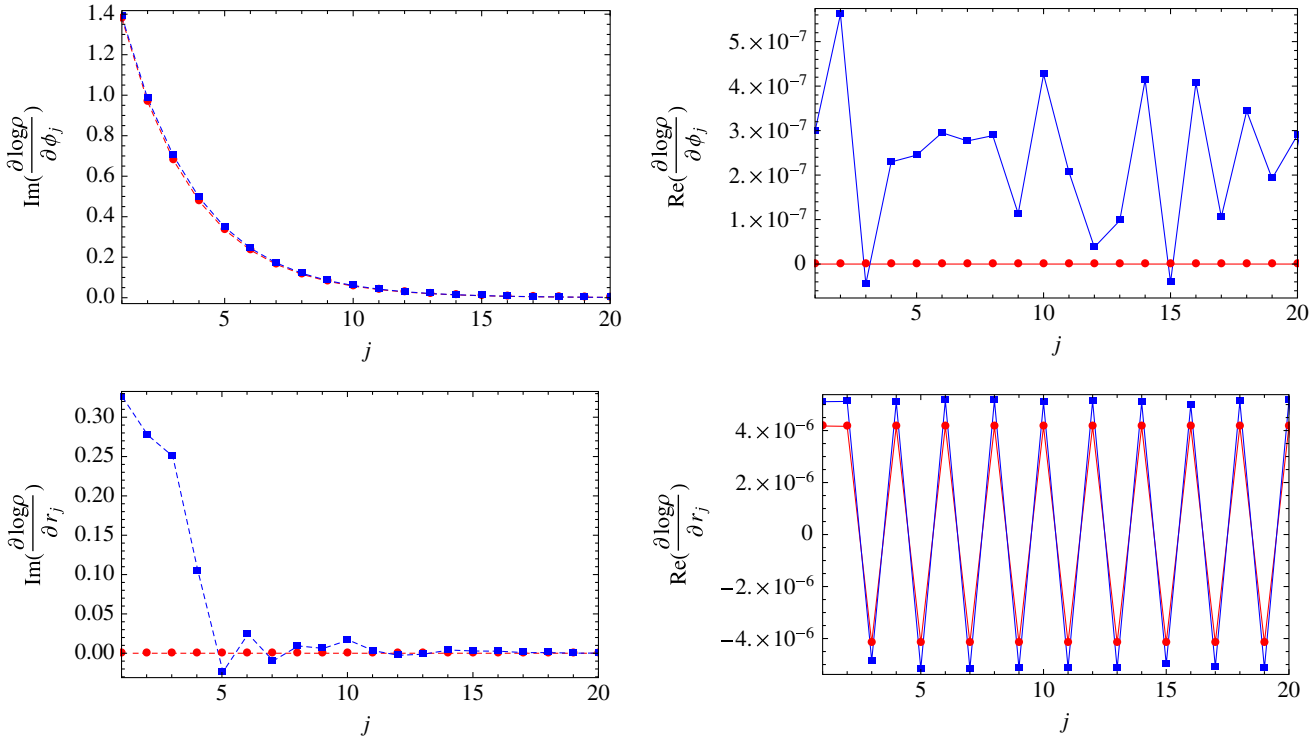

FIG. 5 (color online). Real (solid curves) and imaginary (dashed curves) parts of $\partial \log\rho/\partial\phi_j$ (upper panel) and $\partial \log\rho/\partial r_j$ (lower panel), for conventional (red dots or curves connecting them) and Advanced LIGO (blue squares or curves connecting them) coatings. [Note that $\mathrm{Re}(\partial \log\rho/\partial\phi_j) = 0$ for conventional coating.]

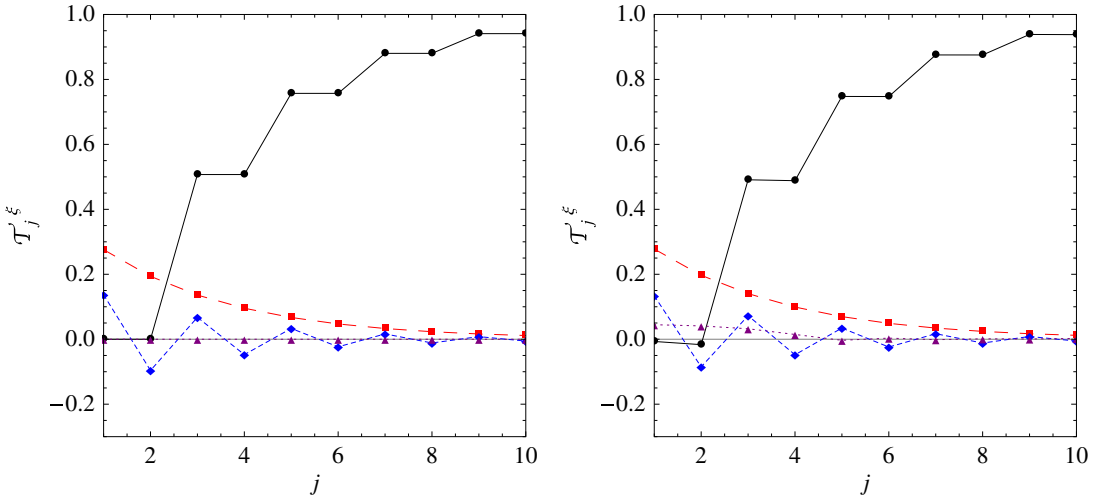

FIG. 6 (color online). Light penetration into the first ten layers of a 38-layer coating (left panel for conventional coating and right panel for Advanced LIGO coating). We plot the nonphotoelastic part of $\mathcal{T}_j$ in black sold curves, the photoelastic part of $\mathcal{T}_j^s$ in long-dashed red curves, as well as $\mathcal{T}_j^s$ (scaled by the rms value of δl_j^c with respect to the rms value of δl_j, shown in short-dashed blue curves) and T_j^s (scaled by the rms value of δl_j^s, shown in dotted purple curves). These plots indicate that for both structures, light penetration is restricted within the first ten layers.

In Eq. (27), we have divided contributions to ξ into four terms: the first, z_s, is the height of the coating-substrate interface, while the other three are related to fluctuations in layer thickness, δl_j, δl_j^c and δl_j^s; see Eqs. (27)–(30). We can illustrate the effect of light penetration by showing the relative size of these three contributions for each layer. In Fig. 6, we carry out this illustration for conventional coating on the left panel and for Advanced LIGO coating on the right. We use a solid black line to indicate the nonphotoelastic part of $\mathcal{T}_j^\xi$ [i.e., terms not containing β_j; see Eq. (28)], and we use long-dashed red, short-dashed blue, and dotted purple curves to indicate the photoelastic parts of $\mathcal{T}_j^\xi$, $\mathcal{T}_j^{\xi c}\sqrt{\langle(\delta l_j^c)^2\rangle/\langle(\delta l_j)^2\rangle}$ and $\mathcal{T}_j^{\xi s}\sqrt{\langle(\delta l_j^s)^2\rangle/\langle(\delta l_j)^2\rangle}$, respectively. The weighting factors,

$$\sqrt{\langle(\delta l_j^c)^2\rangle/\langle(\delta l_j)^2\rangle} = \frac{1}{\sqrt{2}}\sqrt{1+\frac{\sin 4\phi_j}{4\phi_j}}, \tag{103}$$

$$\sqrt{\langle(\delta l_j^s)^2\rangle/\langle(\delta l_j)^2\rangle} = \frac{1}{\sqrt{2}}\sqrt{1-\frac{\sin 4\phi_j}{4\phi_j}}, \tag{104}$$

have been added for $\mathcal{T}_j^{\xi c}$ and $\mathcal{T}_j^{\xi s}$, respectively, to correct for the fact that δl_j^c and δl_j^s have different rms values compared to δl. Because of the lack of experimental data, we have assumed $\beta_j = -0.4$ identically. Note that in order to focus on the effect of light penetration, we have only showed the first ten layers.

In the figure, the effect of light penetration into the coating layers is embodied in the deviation of the solid black curve from unity in the first few layers, and in the existence of the other curves. Although we cannot perceive the correlation between these contributions, we can clearly appreciate that only the first few layers are penetrated, and that the total effect of light penetration will be small. We should also expect the effect of photoelasticity (dashed curves) to be small, and the effect of backscattering (which gives rise to $\mathcal{T}_j^{\xi c}$ and $\mathcal{T}_j^{\xi s}$, dashed blue and purple curves) to be even smaller.

C. Thermal noise contributions from different layers

Let us now examine the breakdown of the total coating noise by plotting the coefficients q_j^B and q_j^S in Eq. (94). In Fig. 7, we plot silica contributions on top panels, and tantala contributions on lower panels, with bulk contributions on left panels, and shear contributions on right panels. Here we use the baseline parameters shown in Table II. As it turns out, the results for conventional and Advanced LIGO coatings are hardly distinguishable from each other—therefore we only use the Advanced LIGO coating. The red curve uses $\beta = -1$, the black uses $\beta = 0$ and the blue uses $\beta = 1$. Superimposed onto the solid lines are dashed lines of each type, calculated without introducing the backscattering terms; the effect is noticeable for the first few layers.

VI. DEPENDENCE OF THERMAL NOISE ON MATERIAL PARAMETERS

Experimental knowledge of coating materials is limited. Most notably, values of Young's moduli and Poisson's ratios of the coating materials are still uncertain, while only *one combination* of the two loss angles has been experimentally measured by ring-down experiments. In this section, we explore the possible variation in coating Brownian noise, away from the baseline configuration (Table II), considering these uncertainties. We shall use

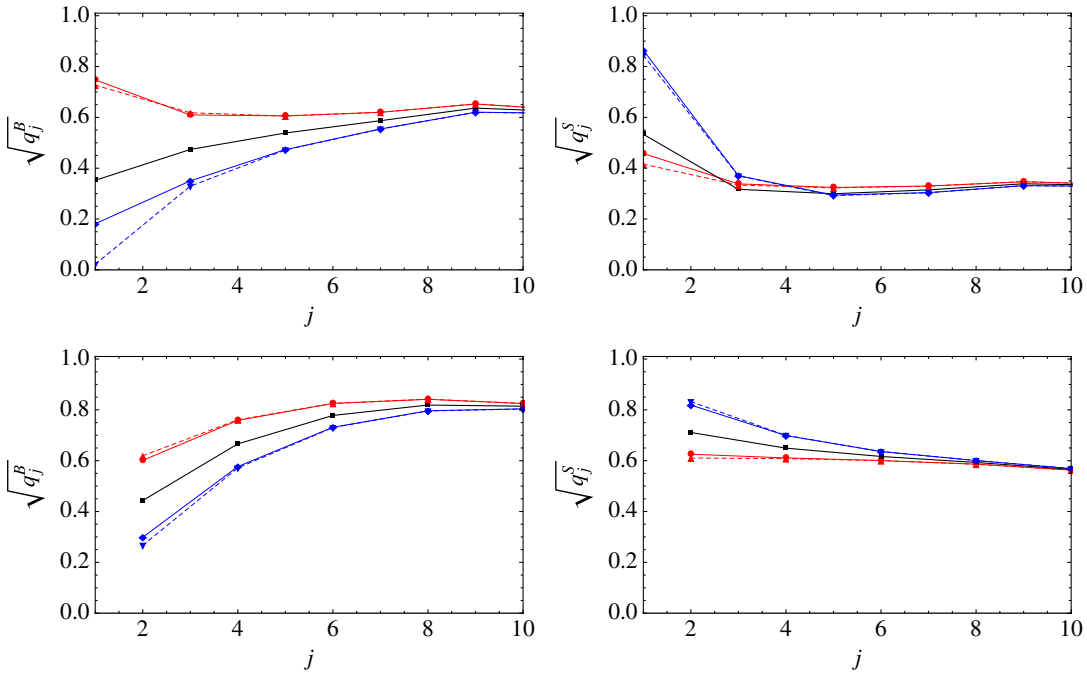

FIG. 7 (color online). A breakdown of thermal noise contributions from silica (upper panels) and tantala (lower panels) layers, and from bulk (left panels) and shear (right panels) losses. Blue curves correspond to $\beta = -1$, black to $\beta = 0$ and red to $\beta = 1$. Dashed curves indicate results calculated without including backscattering effects.

the Advanced LIGO coating structure mentioned in the previous section.

A. Dependence on ratios between loss angles

In the baseline (Table II), we have assumed that ϕ_B and ϕ_S are equal, but this is only out of our ignorance: experiments have only been able to determine one particular combination of these two angles. We now explore the consequence of having these loss angles not equal, while keeping fixed the combination measured by the ring-down rate of drum modes [see Eq. (110)].

In Fig. 8, while fixing all other baseline parameters, we plot how each type of thermal noise (i.e., silica vs tantala, bulk vs shear) varies when the ratio ϕ_B/ϕ_S for both tantala and silica layers varies between 1/5 and 5. We use blue for tantala, red for silica, dotted for bulk, dashed for shear, and solid for the total of bulk and shear. In this configuration, the tantala layers' contribution to thermal noise always dominates over silica layers, mainly due to the higher loss angle. As we vary the ratio between the loss angles, there is moderate variation of thermal noise. For the dominant tantala, as ϕ_B/ϕ_S vary from 1/5 to 5, there is a 30% change in thermal noise, while for silica, the change is a more significant 68%.

As we see from Fig. 8, a larger value of ϕ_B/ϕ_S gives rise to higher bulk, lower shear, and higher total noise—this is reasonable because bulk fluctuations drive correlated noise between a layer's thickness and the height of the coating-substrate interface, while shear fluctuations drive anticorrelated noise, as shown in Fig. 3.

Moreover, the fact that variation is more significant for silica layers can be explained when we recall that thickness-induced thermal noise is proportional to $1/Y_c$, while surface-height-induced thermal noise is proportional to Y_c/Y_s^2. For silica layers, Y_c is assumed to be equal to Y_s, so the two types of noise being added (bulk) or subtracted (shear) are more comparable in magnitude; by contrast, the Young's modulus of tantala layers is significantly higher than that of the substrate, causing the noise to be dominated by fluctuations of the height of the coating-substrate interface, therefore making correlations between the two types of noise less important.

In Fig. 9, we plot variations in the total noise as we vary ϕ_B/ϕ_S for silica layers (blue) or tantala layers (red) only, and fix the other one. It shows that the variance of the tantala's loss angle will generate a larger change in the total noise.

TABLE II. Baseline material parameters.

Parameter	Tantala (Ti_2O_5)	Silica (SiO_2)
Refractive index	2.07 [23]	1.45 [23]
Poisson's ratio	0.23 [24]	0.17 [24]
Young's modulus (Pa)	1.4×10^{11} [25]	7×10^{10} [24]
Loss angle ($\phi_B = \phi_S$)	2.3×10^{-4} [26]	4.0×10^{-5} [27]
Photoelastic coefficient	−0.50 [28]	−0.41 [29]

B. Dependence on Young's moduli and Poisson's ratios

The Young's modulus and Poisson's ratios of coating materials, especially of tantala, are also uncertain.

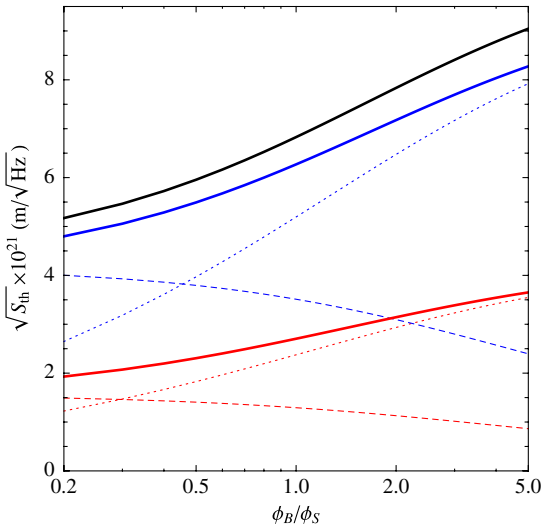

FIG. 8 (color online). Variations in thermal noise contributions when ϕ_B/ϕ_S is varied. Contributions from tantala layers are shown in blue; those from silica layers are shown in red. The total thermal noise is in black. Bulk contributions are shown in dotted curves, while shear contributions are shown in dashed curves.

In Fig. 10, we plot variations of tantala thermal noise when its Young's modulus varies from the baseline value by up to a factor of 2, for $\phi_B/\phi_S = 0.2, 0.5, 1, 2$ and 5. The noise is seen to vary by $\sim$15% as Young's modulus varies by a factor of $\sim$2.

We can also explain the way the thermal noise varies as a function of Y_c. Starting from the baseline value, a lower Y_c leads to a lower thermal noise, until Y_c becomes

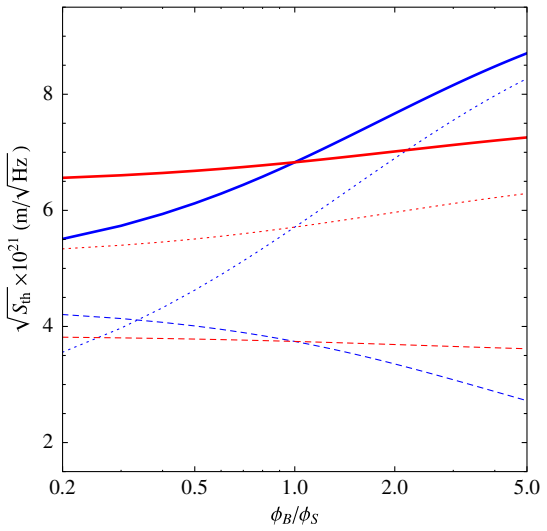

FIG. 9 (color online). Variations in total noise when ϕ_B/ϕ_S is varied: (solid) total noise, (dotted) total bulk noise, (dashed) total shear noise. The red (blue) curve corresponds to only varying ϕ_B/ϕ_S for tantala (silica). With ϕ_B/ϕ_S of tantala or silica varying from 0.2 to 5, the changes in total noise are 58.1% and 10.6% respectively.

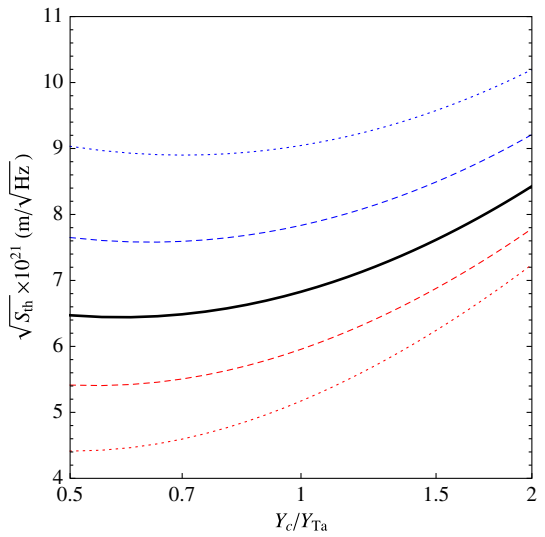

FIG. 10 (color online). Thermal noise contribution from tantala, as its Young's modulus deviates from the baseline value, for $\phi_B/\phi_S = 5$ (dashed blue), 2 (dotted blue), 1 (solid black), 1/2 (dotted red), and 1/5 (dashed red).

comparable to Y_s (which we fix at the baseline value, equal to $0.5Y_{\text{Ta}}$) and starts to increase again. Such a behavior is reasonable because the thickness noise spectrum and interface noise spectrum are proportional to $\sim 1/Y_c$ and $\sim Y_c/Y_s^2$, respectively—as we decrease Y_c from the baseline Y_{Ta} value, we transition from the interface fluctuation being dominant towards an equal amount of both noises (which gives a minimum total noise), and then towards the thickness fluctuation becoming dominant.

In Fig. 11, we explore the effect of varying Poisson's ratio of the tantala coating, for the same values of ϕ_B/ϕ_S

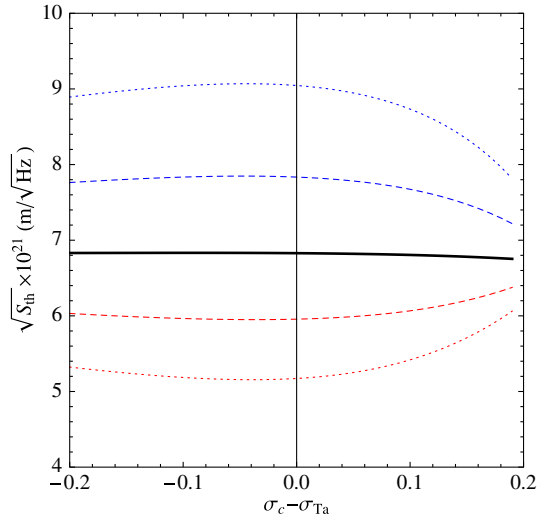

FIG. 11 (color online). Thermal noise contribution from tantala, as its Poisson's ratio deviates from baseline value, for $\phi_B/\phi_S = 5$ (dashed blue), 2 (dotted blue), 1 (solid black), 1/2 (dotted red), and 1/5 (dashed red).

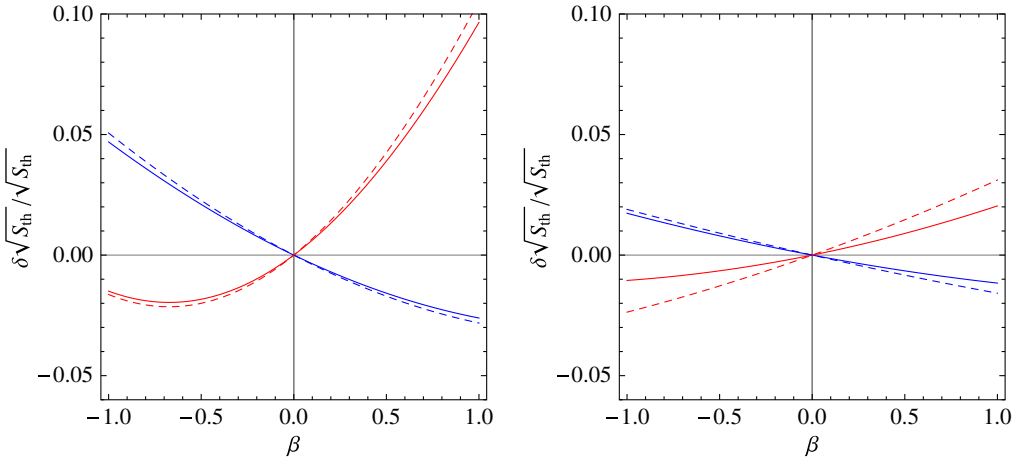

FIG. 12 (color online). Fractional change in the contribution to thermal noise from all silica layers (left panel) and all tantala layers (right panel), due to bulk (blue) and shear (red) loss. Dashed lines indicate results calculated without including backscattering terms.

chosen in Fig. 10. In the baseline assumption of $\phi_B = \phi_S$, when bulk and shear have the same level of loss, thermal noise does not depend much on Poisson's ratio. However, if ϕ_B/ϕ_S turns out to differ significantly from 1, and if Poisson's ratio can be larger than the baseline value by more than ~ 0.1, then thermal noise can vary by $\sim 10\%$.

C. Dependence on photoelastic coefficients

Photoelastic properties of the coating materials are not yet well known. In Fig. 12, we plot the fractional change in thermal noise, separately for silica (left panel) and tantala (right pane), and for bulk (blue) and shear (red) losses, when we vary β between -1 and $+1$. Dashed curves are obtained, ignoring backscattering effects.

It is interesting to note that for small values of β, the dependences of noise on β have different trends for bulk and shear contributions. This is also related to the different types of correlations between thickness and interface height fluctuations. As we can see from the figure, the effect of varying β is small, since it only affects thermal noise due to light penetration into the first few layers. If bulk and shear losses are indeed comparable, then cancellation between these two types of noises (especially for the tantala layers which are more lossy than silica layers) will likely make the photoelastic effect completely negligible. Even in the case when one particular type of loss dominates shall we expect at most $\sim 2\%$ contribution from photoelasticity of the more lossy tantala—if we further assume that $|\beta| \sim 1$ [right panel of Fig. 12].

D. Optimization of coating structure

Although a standard highly reflective coating consists of $\lambda/4$ layers of alternating material capped by a $\lambda/2$ layer, this structure can be modified to lower thermal noise while still maintaining a high reflectivity for the 1064 nm carrier light, e.g., as shown by Agresti *et al.* [30]. As their results have indicated, using baseline coating parameters and neglecting light penetration into the coating layers [14], the optimal structure is closer to a stack of pairs of $\lambda/8$ (Ta_2O_5) and $3\lambda/8$ (SiO_2) layers, capped by a $\lambda/2$ (SiO_2) layer. This alternative coating structure shortens the total thickness of the more lossy tantala layers, while maintaining a high reflectivity for the light. The *Advanced LIGO type* coating given in Appendix D, on the other hand, has been optimized considering reflectivity at both 1064 nm and 532 nm, as well as thermal noise—although light penetration into the layers has not been considered.

In this section, we carry out a numerical optimization taking penetration into account. We first fix the number N of layers (N is even, so we have $N/2$ pairs), and then for N, we use the Lagrange multiplier method to search for the constrained minimum of $S_{\rm th}$, fixing T_{1064} and T_{532}, namely the power transmissivity, $1 - |\rho|^2$ assuming the coating is lossless, evaluated at 1064 nm and 532 nm, respectively. The quantity we seek to minimize (or, the *cost function*) is

$$y \equiv \sqrt{S_{\rm th}} + \mu_1 T_{1064} + \mu_2 (T_{532} - 5\%)^2. \qquad (105)$$

As we vary μ_1 and μ_2 and minimize y, we obtain the constrained minimum of $\sqrt{S_{\rm th}}$ for different pairs of (T_{532}, T_{1064}). The aim is to obtain a series of coating configurations with approximately 5% transmissivity for 532 nm, and with minimized thermal noise for a variable 3–20 ppm transmissivity for 1064 nm. (Note that the choice of the cost function contains a certain level of arbitrariness.)

Since we are going to carry out minimization for a large number of multipliers over a large number of degrees of freedom, we have chosen to proceed gradually, allowing only the first n pairs and last n pairs of layers to vary, while maintaining the same pair structure for $N/2 - n$ pairs in the middle (repeating doublets). In other words, our coating structure looks like

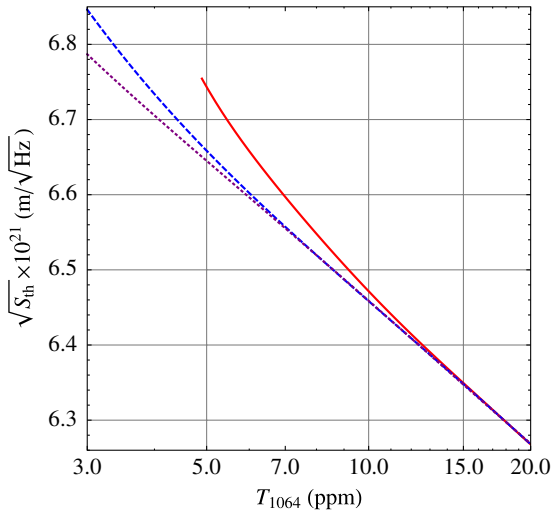

FIG. 13 (color online). Optimized thermal noise versus transmissivity at 1064 nm, for a coating of 38 (red), 40 (blue), and 42 (purple) layers.

$$\underbrace{\text{free}}_{2n\text{ layers}}\ \underbrace{\text{repeating pair}}_{N-2n\text{ layers}}\ \underbrace{\text{free}}_{2n\text{ layers}}.$$

In this work, we found that it suffices to choose $n = 2$ (which corresponds to optimizing over ten parameters); further increasing n does not lead to noticeable improvements. During our numerical optimization, we have adopted the *downhill simplex method* [31,32].

Results for baseline material parameters (Table II) and $N = 38$, 40 and 42 have been shown in Fig. 13. This figure indicates that different numbers of layers should be chosen for different target T_{1064}—more layers are required for lower transmissivity (higher reflectivity). Overall, the optimal thermal noise varies by around $\sim 10\%$ as for T_{1064} from 3 to 20 ppm. In particular, for the standard Advanced LIGO requirement of 5 ppm (see the first column of Table III), 42 layers are found to be optimal. This is two more pairs or four more layers than the 38-layer $\lambda/4$ doublet, which has the minimum number of layers to reach 5 ppm. The larger number of layers here gets lower thermal noise (by 6%) because the more lossy tantala layers are shortened, and the less lossy silica layers lengthened.

We have further optimized the structure when the ratio ϕ_B/ϕ_S is different from 1, while keeping fixed the effective loss angle measured so far—as done in Sec. VI A. For $T_{1064} = 5$ ppm, we have listed the results of an optimized coating structure and thermal noise in the second and third columns of Table III. The extent of variation found here is comparable to that obtained in Sec. VI A using a standard coating structure without optimization: the optimal coating structures consistently lower thermal noise by about 6%. In addition, as shown in Table III, the optimal coating structure is robust against changes in ϕ_B/ϕ_S: structure obtained for any one of the values of the ratio is already almost optimal for all other ratios.

VII. MEASUREMENTS OF LOSS ANGLES

In this section, we study possible mechanical ring-down experiments that can be used to measure independently the bulk and shear loss angles, ϕ_B and ϕ_S of a coating material.

In a ring-down experiment, a sample with a high intrinsic Q is coated with a thin layer of the coating material in question. Due to the mechanical losses in the coating, the quality factor of the mechanical eigenmodes of the sample will be reduced [33,34]. More specifically, for the nth eigenmode with resonant frequency f_n, if an e-folding decay time of τ_n is measured, then the quality factor is

$$Q_n = \pi f_n \tau_n, \tag{106}$$

while correspondingly, the loss angle is given by

$$\phi(f_n) = 1/Q_n, \tag{107}$$

which is equal to the fraction of energy dissipated per radian.

A. Bending modes of a thin rectangular plate

Figure 14 shows the schematic geometry of a rectangularly shaped sample, in which a thin coating layer with thickness d is deposited on a rectangular plate with dimensions $a \times b \times c$ ($c \ll a, b$), and d is much less than c. If we pay attention only to the bending (or, in other words, flexing) oscillations of the plate, the amount of energy

TABLE III. Results of coating-structure optimization. We list optimized coating structures for $T_{1064} = 5$ ppm and $T_{532} = 5\%$, for three target values of ϕ_B/ϕ_S while fixing the measured effective loss angle ϕ_D [Eq. (56)] and other baseline material parameters (Table II). Thicknesses of coating layers are given in units of wavelength (for 1064 nm light). For each optimized coating structure, thermal noise is calculated separately for the same three values of ϕ_B/ϕ_S, and given in units of 10^{-21} m/$\sqrt{\rm Hz}$ (thermal noise for the target ϕ_B/ϕ_S is given in boldface, and boldface numbers should be the minimum within its column); thermal noise spectra of the 38-layer $\lambda/4$ stack assuming the target ϕ_B/ϕ_S are also listed for comparison.

Target		Resulting coating structure										$\sqrt{S_{\rm th}^{\rm opt}}$			$\sqrt{S_{\rm th}^{\lambda/4}}$
ϕ_B/ϕ_S	N	First 4 layers				Repeated pair		Last 4 layers				$\frac{\phi_B}{\phi_S} = \frac{1}{5}$	$\frac{\phi_B}{\phi_S} = 1$	$\frac{\phi_B}{\phi_S} = 5$	
1/5	42	0.0479	0.1581	0.3430	0.1760	0.2919	0.1897	0.3164	0.1738	0.3178	0.1627	5.01	6.64	8.81	5.35
1	42	0.1020	0.1250	0.3267	0.1917	0.2911	0.1914	0.3110	0.1752	0.3196	0.1609	5.02	6.64	8.81	7.05
5	42	0.1118	0.0968	0.3353	0.1882	0.2893	0.1939	0.3135	0.1673	0.3199	0.1662	5.02	6.64	8.81	9.33

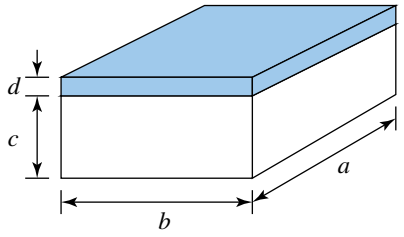

FIG. 14 (color online). Rectangular shaped thin plate ($a \times b \times c$) with thin coating (thickness d): $c \ll a$, b; $d \ll c$. The transverse vibration mode is considered in this case.

stored in the coating layer, in the form of bulk and shear energies U_B and U_S, as a fraction of the entire energy U, can be calculated as

$$\frac{U_B}{U} = \frac{d}{3c}\frac{Y_c}{Y_s}\frac{(1-\sigma_s^2)(1-2\sigma_c)}{(1-\sigma_c)^2} \tag{108}$$

$$\frac{U_S}{U} = \frac{2d}{3c}\frac{Y_c}{Y_s}\frac{(1-\sigma_s^2)(1-\sigma_c+\sigma_c^2)}{(1-\sigma_c)^2(1+\sigma_c)}. \tag{109}$$

Using Eq. (58), the total loss angle of the sample is

$$\begin{aligned}\phi &= \phi_{\text{sub}} + \frac{d}{c}\frac{Y_c}{Y_s}\frac{1-\sigma_s^2}{1-\sigma_c^2} \\ &\quad\times\left[\frac{\phi_B(1-\sigma_c-2\sigma_c^2)+2\phi_S(1-\sigma_c+\sigma_c^2)}{3(1-\sigma_c)}\right] \\ &= \phi_{\text{sub}} + \frac{|D_c|}{|D_s|}\phi_D.\end{aligned} \tag{110}$$

It is not surprising that only the 2D flexural rigidity D and its imaginary part appear in Eq. (110). During the bending of a thin plate with thin coating, both the substrate and the coating are described by the 2D flexural rigidity, first introduced in Sec. III B [see Eqs. (55) and (56) and Sec. 13 of Ref. [18]]. Because they both bend in the same way, the ratio of their elastic energies is given directly by the ratio of their flexural rigidities (each proportional to their thickness). The fraction of total energy lost in the coating needs to be multiplied by ϕ_D (of the coating material), and hence Eq. (110). As the oscillation of a thicker object is considered, as long as the coating only bends up and down (e.g., in a drum mode), then we expect the coating contribution to the loss angle to still be proportional to ϕ_D.

As it turns out, the part of coating thermal noise due to bending of the coating-substrate interface [$S_{z_s z_s}$ in Eq. (87b)] also depends directly on ϕ_D, because the loss mechanism in this case is the same as that during the oscillation of a drum mode—one only applies a perpendicular force from below the coating layer, while keeping $T_{zz} = 0$ within the layer.

It proves less straightforward to connect the thickness fluctuation part of thermal noise [$S_{u_z u_z}$ in Eq. (87a)] to the effective loss angle of either Y or D. Although the loss mechanism here is due to the compressing of a thin membrane from both sides, this membrane is not characterized by vanishing T_{xx} and T_{yy}, because the coating is attached to a substrate which provides restoring forces along the transverse (x and y) directions. However, in the case when the Poisson's ratio σ_c of the coating vanishes, the thickness fluctuation does depend on the loss angle of the Young's modulus.

For our baseline parameters, mechanical dissipation is mostly contributed by the tantala layers, and because the Young's modulus of the tantala coating material is assumed to be much greater than that of the substrate, the largest contribution to the LIGO mirrors' Brownian noise is bending noise $S_{z_s z_s}$. This explains why the noise only varies by 30% (as noted in Sec. VI A) even if no further measurements on the other loss angle are made.

B. Torsional modes of a coated hollow cylinder

Here we propose an approach with which we can measure another combination of loss angles. We consider a cylindrical shell with a thin, uniform coating layer outside, as shown in Fig. 15 ($c \ll R$, $d \ll c$). In this configuration, the surface deformations produce strains in the plane of the shell according to the Donnell shell theory [35]. Here we assumed that there is only angular displacement in the shell, which means the longitudinal position of the cross section will not change. For a torsion mode, we only have shear strain energy; the expressions are given by

$$\frac{U_B}{U} = 0 \tag{111}$$

$$\frac{U_S}{U} = \frac{d}{c}\frac{Y_c}{Y_s}\frac{(1+\sigma_s)}{(1+\sigma_c)}. \tag{112}$$

As a consequence, the total loss angle can be expressed as

$$\phi = \phi_{\text{sub}} + \frac{d}{c}\frac{Y_c}{Y_s}\frac{(1+\sigma_s)}{(1+\sigma_c)}\phi_S. \tag{113}$$

For a cylinder shell, according to the Donnell shell theory, the natural frequency of the nth torsional mode is given by [36]

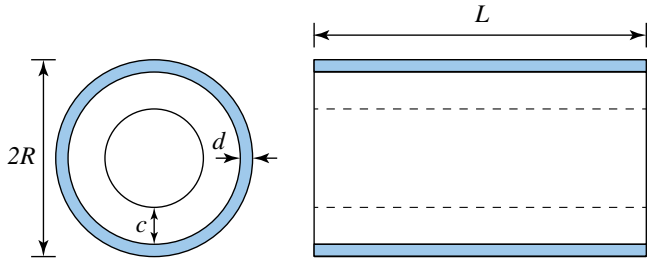

FIG. 15 (color online). Thin cylindrical shell with thin coating outside. The first torsional eigenmodes of such a shell can be used to measure the shear loss angle of the coating.

TABLE IV. Example parameters of a thin, uniformly coated cylindrical shell (SiO_2).

	L	R	c	d
Unit (mm)	200	50	1	0.04

$$f_n = \frac{n}{2\pi L}\left[\frac{Y}{\rho(1+\sigma)}\right]^{1/2}. \tag{114}$$

A more accurate calculation may be found by using the Flügge shell theory [37].

Using the values from Table IV, we can estimate the resonant frequency to be 9.2 kHz. The coating contribution to the loss angle, assuming a ϕ_S of at least 10^{-5}, would be at least of the order of 10^{-6}, which seems plausible to be extracted from ring-down measurements.

With the measurement of both the thin plate and cylinder shell, we can obtain ϕ_B and ϕ_S of the coating.

VIII. CONCLUSIONS

In this paper, we applied the fluctuation-dissipation theorem to obtain a *full set of correlation functions* (87a)–(87c) of Brownian thermal fluctuations of a multilayer dielectric coating. In particular, we have related fluctuations of the coating thickness and the coating-substrate interface to *independent* bulk and shear thermal stresses associated with each coating layer. While those stresses not only induce thickness fluctuations of the layers themselves, they bend the coating-substrate interface and this bending noise had not been previously appreciated intuitively, although its effect has been incorporated into formulas, e.g., in Ref. [14]. As a result, we found that although thickness fluctuations of different coating layers are independent of each other, they each have partial correlations with the height fluctuations of the coating-substrate interface. Moreover, bulk loss creates a positive correlation between them, while shear loss creates a negative correlation. The entire picture is succinctly written mathematically in Eqs. (89) and (90). This coherence structure then gives coating Brownian noise in Eq. (93). Apart from having provided a pedagogical and systematic derivation of these noise components, the most important conceptual consequence of our work is to point out an uncertainty in coating loss angles. We have also incorporated the photoelastic effect, the reflectivity fluctuations of the interfaces within the multilayer coating, and considered the effect of amplitude modulations caused by Brownian thermal noise. All of these turned out to be rather unimportant.

We have applied our formalism to mirrors that are to be used in Advanced LIGO detectors. As estimated in Sec. VI and summarized in Table V (calculated for a typical candidate for the Advanced LIGO end test-mass mirror coating configuration), parameter uncertainties could lead to non-negligible corrections to coating Brownian noise calculations. The biggest uncertainties actually arise from the elastic moduli of coating materials—for example, current uncertainties in Young's modulus of the tantala coating material might lead to up to a 60% increase in thermal noise. Although photoelastic coefficients for our coating materials are very uncertain, they do not significantly affect thermal noise since light does not penetrate through many layers.

It is rather remarkable that our lack of experimental knowledge about the loss angles, beyond what we had already obtained from the ring down of drum modes, would not give rise to a higher uncertainty in thermal noise. This is rather serendipitous, considering our path of understanding of the problem: for the baseline parameters of Advanced LIGO, the highest contribution to coating Brownian noise arises from the coating-substrate bending noise caused by losses in tantala layers, because these layers are much more lossy than the silica layers, and have been assumed to have a much higher Young's modulus than the substrate material. This bending noise, first elaborated by this work, turns out to be associated with the loss angle of the 2D flexural rigidity, which in turn is directly connected to the decay of the drum modes of a thinly coated sample. This means the currently existing program [14] has been measuring the predominant loss angle all along, and has been compatible with direct measurements of coating thermal noise [15]. Nevertheless, the level of uncertainty noted in our study still warrants further experiments seeking the other loss angle, e.g., as outlined in Sec. VII. In addition, since future gravitational-wave detectors may use different substrate and coating materials, situations may arise when the loss angle measured now does not correlate with the total coating Brownian noise.

At this moment, it is worth looking once more at the previously used loss angles, $\phi_\parallel$ and $\phi_\perp$—although they are mathematically ill defined, they do correctly reflect the existence of two channels of loss. The $\phi_\parallel$ was meant to

TABLE V. Levels of thermal noise uncertainty caused by parameter uncertainties.

Material parameter	Range	Uncertainty in $\sqrt{S_x}$	For details, see
ϕ_B/ϕ_S	0.2–5[a]	±37%	Sec. VI A, Figs. 8 and 9
Y_{Ta}	Factor of ~2	~60%	Sec. VI B, Figs. 10
σ_{Ta}	±0.2	Up to 10% if $\phi_B/\phi_S \neq 1$	Sec. VI B, Figs. 11
β	$-1 < \beta < +1$	±1%[b]	Sec. VI C, Figs. 12

[a]Fixing the combination ϕ_D.
[b]Calculated from Ta_2O_5 layers.

TABLE VI. Comparison of thermal noise spectral density (assuming $\phi_B = \phi_S$ and evaluated at 200 Hz, in units of 10^{-21} m/$\sqrt{\text{Hz}}$) among different works.

Coating	Ref. [14] (no light penetration)	Ref. [17] ($\beta = 0$ and no backscattering)	This work
$\lambda/4$	7.18	7.08	7.08
Advanced LIGO	6.93	6.82	6.83
Optimal	6.73	6.62	6.64

characterize losses incurred by the x-y deformations of the coating measurable when we do not compress the coating but instead drive its deformations using drum modes of the substrate. This loss angle is now replaced by the (mathematically well-defined) imaginary part of the flexural rigidity, for which extensive measurements have already been carried out. The $\phi_\perp$ was meant to characterize the losses incurred by compressing the coating layers. This has not been measured because it had not been obvious how to easily excite this mode of coating deformation (the most obvious way would be to compress the coating layer, but that is difficult); however, because the Young's modulus of the coating is much larger than that of the substrate, this difficult-to-measure loss angle should not contribute as much to the total coating noise. This said, in this work, we do come up with ways to measure both loss angles, ϕ_S and ϕ_B, without having to compress the coating layers—but instead by exciting different modes of substrate deformation. Of course, this is only possible because we have assumed that the material is isotropic—otherwise we may have to compress the coating to directly access the loss induced by such a deformation.

On the other hand, one may think of the possibilities of using substrate materials with a higher Young's modulus to reduce the bending noise. Sapphire and silicon are two viable choices because they both have a higher Young's modulus than tantala. Using Eqs. (87a)–(87c), it is straightforward to estimate the new coating Brownian noise while replacing the substrate material by sapphire or silicon but keeping the same aLIGO coating design. It turns out that the coating Brownian noise will be reduced to 35% of its original power spectra value if we use silicon substrate or 32% if we use sapphire. However, there are other disadvantages for sapphire or silicon substrate that prevent us from using them for aLIGO mirrors. The main problem is that they both have very high thermal conductivity—much higher than fused silica. As a result, the substrate thermoelastic noise is one of the important noise sources for both materials. For instance, if the aLIGO mirror were made of sapphire, the bulk thermoelastic noise would have about the same magnitude as the coating Brownian noise at 100 Hz. As for silicon substrate, the bulk thermoelastic noise is more than twice as large as its corresponding coating Brownian noise because silicon has even higher thermal conductivity than sapphire. One may refer to [38] for detailed methods to calculate bulk thermoelastic noise. Setting up the experiment in a cryogenic environment is a possible way to reduce the thermo-optic noise.

Furthermore, our formula Eq. (93) can serve as a starting point for optimizing the material choice and structure design of the multilayer coating, taking light penetration effects into account. Our numerical results in Sec. VI D (see Table III) have shown that optimization of the coating structure consistently offers a ~6% decrease in thermal noise, regardless of ϕ_B/ϕ_S. In fact, the optimal structures for these ratios are quite similar, and configurations obtained for each presumed ratio of ϕ_B/ϕ_S are shown to work for other ratios interchangeably.

Upon completion of this manuscript, we noted that the optimization of the coating structure for the case assuming $\phi_B = \phi_S$ (and $\beta = 0$) has been carried out by Kondratiev *et al.* [17]. (We note that their formalism is capable of treating $\beta \neq 0$ and $\phi_B \neq \phi_S$, as well as backscattering induced by photoelasticity, but they did not explore the impact of these effects in their optimization.) Our results are compatible with theirs, if we also use these restrictions in parameter space and ignore backscattering.

A comparison between our result, Kondratiev *et al.*, and Harry *et al.* [14] (which ignores light penetration into the layers, and also effectively assumes $\phi_S = \phi_B$) would therefore illustrate the effects caused by ignoring photoelasticity and further ignoring light penetration into the coating. This is shown in Table VI. This again confirms that for total coating thermal noise, light penetration causes a noticeable difference in coating thermal noise, while photoelasticity causes a negligible difference.

ACKNOWLEDGMENTS

We would like to thank Stan Whitcomb, Raffaele Flaminio, Jan Harms, Gregg Harry, Yasushi Mino, Valery Mitrofanov, Kentaro Somiya, Sergey Vyatchanin, and other members of the LSC Optics Working Group for very useful discussions. We thank Iain Martin and Andri Gretarsson for many useful suggestions for the manuscript. This work was supported by NSF Grants No. PHY-0757058, No. PHY-1068881 and CAREER Grant No. PHY-0956189, the David and Barbara Groce Startup Fund, and the David and Barbara Research Assistantship at the California Institute of Technology. Funding has also been provided by the Institute for Quantum Information and Matter, a NSF Physics Frontiers Center with support of the Gordon and Betty Moore Foundation.

APPENDIX A: FLUCTUATIONS OF THE COMPLEX REFLECTIVITY DUE TO REFRACTIVE INDEX FLUCTUATIONS

Brownian noise is not only caused by random strains, but also by the refractive-index fluctuations induced by such strains through the photoelastic effect [cf. Eqs. (13) and (14)]. We will quantify this contribution in this section.

1. The photoelastic effect

If we denote the displacement of coating mass elements as (u_x, u_y, u_z), then the relative coating-thickness change from its equilibrium value can be written as

$$\delta l/l = u_{z,z} \tag{A1}$$

and the relative transverse area expansion can be written as

$$\delta A/A = u_{x,x} + u_{y,y}. \tag{A2}$$

If we denote two-dimensional displacement vectors along the x-y plane as $\vec{u} = (u_x, u_y)$, and the two-dimensional gradient as $\vec{\nabla}$, then we have

$$\delta A/A = u_{x,x} + u_{y,y} = \vec{\nabla} \cdot \vec{u}. \tag{A3}$$

We can then write the change in refractive index as

$$\delta n = \left[\frac{\partial n}{\partial \log l}\right]_{A_j} \frac{\delta l}{l} + \left[\frac{\partial n}{\partial \log A}\right]_{l_j} \vec{\nabla} \cdot \vec{u} \tag{A4}$$

where $\partial n/\partial \log l$ and $\partial n/\partial \log A$ only depend on material properties. The two terms on the right-hand side of Eq. (A4) represent the refractive index change driven by relative length and area changes, respectively. The first term is given by [29]

$$\beta^L = \left[\frac{\partial n}{\partial \log l}\right]_A = -\frac{1}{2} n^3 CY \tag{A5}$$

where C is the photoelastic stress constant, and Y is the Young's modulus. For silica, $CY \approx 0.27$; therefore $\beta^{\mathrm{L}}_{\mathrm{SiO_2}} = -0.41$. The photoelastic coefficient can also be written as

$$\beta = -\frac{1}{2} n^3 p_{ij} \tag{A6}$$

where p_{ij} is the photoelastic tensor [39]. Some experiments have been done to measure this coefficient for tantala [28]. Empirically, the value of p_{ij} varies from -0.15 to 0.45 for Ta_2O_5 thin film fabricated in different ways. Here for the longitudinal photoelasticity, $\beta^{\mathrm{L}}_{\mathrm{Ta_2O_5}}$, we use -0.5 in our numerical calculation.

We shall next obtain formulas that will allow us to convert fluctuations in n into fluctuations in the complex reflectivity of the multilayer coating.

2. Fluctuations in an infinitesimally thin layer

Because the coating is very thin compared with the beam spot size, we model the phase shift of light gained during propagation along z as only determined by the local refractive index. If the refractive index δn at a particular location $\delta n(z)$ is driven by longitudinal strain u_{zz} at that location, the fact that $\langle u_{zz}(z') u_{zz}(z'') \rangle \propto \delta(z' - z'')$ causes concern, because this indicates a high *variance* of δn at any given single point z, with a magnitude which is formally infinity. If we naively consider the reflection of light across any interface within the coating, e.g., at $z = z_0$, then the independent and high-magnitude fluctuations of $n(z_0-)$ and $n(z_0+)$ would lead to a dramatic fluctuation in the reflectivity

$$r = \frac{n(z_0-) - n(z_0+)}{n(z_0+) + n(z_0-)} \tag{A7}$$

because, naively, $n(z_0-)$ and $n(z_0+)$ are uncorrelated and both have a variance of infinity.

However, two effects prevent the above divergence from actually taking place: (i) there is a finite correlation length for strain fluctuations (although not explicitly given in our current analysis) and (ii) propagation of light averages over those fluctuations. The most convenient way to circumvent the above divergence is to always consider light propagation across a finite layer of materials. As shown in Fig. 16, let us consider three regions in the coating, with refractive indices n_1, n_2 and n_3 separated by two interfaces, with the length of the n_2 layer given by Δl—and here we only consider fluctuations in n_2. The entire transfer matrix (Fig. 16) is given by

$$\mathbf{M} = \mathbf{R}_{r_{12}} \mathbf{T}_{\phi_2} \mathbf{R}_{r_{23}} \tag{A8}$$

following the same convention as in Sec. II C. Suppose the originally uniform n_2 now fluctuates, and after averaging over this think layer, gives a mean refractive index of $n_2 + \delta n_2$; we use this as the refractive index of the entire layer, and then have

$$\delta \mathbf{M} = \frac{n_2}{\sqrt{n_1 n_3}} \begin{pmatrix} i & -i \\ i & -i \end{pmatrix} \delta n_2 \cdot k_0 \Delta l. \tag{A9}$$

Note that when $\Delta l \to 0$, $\delta n_2 \cdot \Delta l$ has a variance that approaches zero, and therefore $\delta \mathbf{M}$ is an infinitesimal matrix—and there is no divergence. [Note that when Δl is small enough, δn_2 has a variance that is comparable to the total variance of n, which is finite—therefore $\delta n_2 \cdot \Delta l \sim O(\Delta l)$.]

The physical meaning of Eq. (9) is the following: a random field of refractive index not only gives rise to a

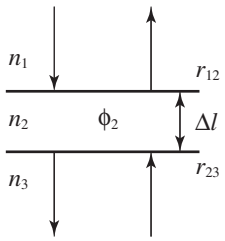

FIG. 16. Light propagation across a thin layer (thickness of Δl) with fluctuating refractive index (from a uniform n_2 to an average of $n_2 + \delta n_2$ within this thin layer). The propagation matrix corresponding to this structure is given by Eq. (8).

random phase shift (diagonal term), but also gives rise to a random reflectivity (nondiagonal term). The latter term is an additional contribution that has been ignored by previous analytical calculations.

3. The entire coating stack

Now we are ready to consider the entire multilayer coating. Let us first focus on layer j of the coating stack, bounded by two interfaces with reflectivities r_{j-1} and r_j, respectively. Since the total transfer matrix of the entire stack is written as

$$\mathbf{M} = \cdots \mathbf{T}_{\phi_{j+1}} \mathbf{R}_{r_j} \mathbf{T}_{\phi_j} \mathbf{R}_{r_{j-1}} \cdots, \tag{A10}$$

the reflectivity fluctuations with this layer will contribute to the matrix $\mathbf{T}_{\phi_j}$ above, which in turn will contribute to fluctuations in the entire $\mathbf{M}$. Consider a dz-thick sublayer located at distance z' from the r_j boundary (lower boundary in Fig. 1), therefore at coordinate location $z = z_{j+1} + z'$, and integrate; we have

$$\mathbf{T}_{\phi_j} \rightarrow \mathbf{T}_{\phi_j} + k_0 \int_0^{l_j} \delta n(z_{j+1}+z) \mathbf{T}_{k_0 n_j z} \begin{bmatrix} i & -i \\ i & -i \end{bmatrix} \times \mathbf{T}_{k_0 n_j (l_j - z)} dz' = \begin{bmatrix} 1 & \delta\eta_j \\ \delta\eta_j^* & 1 \end{bmatrix} \mathbf{T}_{\phi_j + k_0 \delta\bar{n}_j l_j} \tag{A11}$$

where

$$\delta\bar{n}_j = \frac{1}{l_j} \int_0^{l_j} \delta n_j(z_{j+1}+z) dz \tag{A12}$$

and

$$\delta\eta_j = -ik_0 \int \delta n_j(z_{j+1}+z) e^{2ik_0 n_j z} dz. \tag{A13}$$

Here we have defined

$$z_j \equiv \sum_{n=j}^{N} l_n \tag{A14}$$

to be the z coordinate of the top surface of layer j.

We need to adapt the new transfer matrix into the old form, but with modified $\{r_j\}$ and $\{\phi_j\}$. From Eq. (11), since $\delta\eta_j$ is complex, we need to adjust ϕ_j, r_j, as well as ϕ_{j+1}:

$$\mathbf{T}_{\phi_{j+1}} \mathbf{R}_{r_j} \mathbf{T}_{\phi_j} \rightarrow \mathbf{T}_{\phi_{j+1} + \delta\psi_j^+} \mathbf{R}_{r_j + \delta r_j} \mathbf{T}_{\phi_j + k_0 l_j \delta\bar{n}_j + \delta\psi_j^-}. \tag{A15}$$

Here we have defined in addition

$$\delta r_j = -t_j^2 k_0 \int_0^{l_j} \delta n_j(z_{j+1}+z) \sin(2k_0 n_j z) dz \tag{A16}$$

and

$$\delta\psi_j^{\pm} = \frac{r_j^2 \pm 1}{2r_j} k_0 \int_0^{l_j} \delta n_j(z_{j+1}+z) \cos(2k_0 n_j z) dz. \tag{A17}$$

As we consider the photoelastic noise of all the layers together, δr_j in Eq. (16) needs to be used for the effective fluctuation in reflectivity of each layer, while

$$\delta\phi_j = k_0 l_j \delta\bar{n}_j + \delta\psi_j^- + \delta\psi_{j-1}^+ \tag{A18}$$

should be used as the total fluctuation in the phase shift of each layer.

4. Unimportance of transverse fluctuations

Connecting with the photoelastic effect, the refractive index change is

$$\delta n_j(z, \vec{x}) = \beta_j^L u_{zz}(z, \vec{x}) + \beta_j^T \vec{\nabla} \cdot \vec{u}. \tag{A19}$$

Here the vector $\vec{u}$ is the two-dimensional displacement vector (u_x, u_y) and $\vec{\nabla}\cdot$ is the 2D divergence along the x-y plane. For terms that contain the transverse vector $\vec{u}$, we note that when a weighted average of ξ is taken over the mirror surface (see Sec. II D), they yield the following type of contribution:

$$\int_M I(\vec{x})(\vec{\nabla}\cdot\vec{u}) d^2\vec{x} = \int_{\partial M} dl(\vec{n}\cdot\vec{u}I) + \int_M \vec{u}\cdot\vec{\nabla} I d^2\vec{x} = \int_M \vec{u}\cdot\vec{\nabla} I d^2\vec{x}. \tag{A20}$$

Here M stands for the 2D region occupied by the beam, and ∂M is the boundary on which power vanishes. As a consequence, the first term is zero according to the boundary condition, while the second term gains a factor of (l_i/w_0) with respect to other types of coating Brownian noise; here l_j is the thickness of the jth layer, and w_0 the beam spot size. Since we always assume coating thickness l_i to be much smaller than the beam radius r_{beam}, we can neglect refractive index fluctuation due to area fluctuation.

APPENDIX B: ELASTIC DEFORMATIONS IN THE COATING

Throughout this paper, we assume the mirror substrate to be a half infinite space. We establish a Cartesian coordinate system, with (x, y) directions along the coating-substrate interface, and z direction orthogonal to the mirror surface (in the elasticity problem, we also ignore mirror curvature). This allows us to calculate elastic deformations in the spatial frequency domain. We will also assume the coating thickness to be much less than the beam spot size.

We denote the displacement along x, y and z directions as u_x, u_y and u_z. It is then straightforward to express the 3×3 strain tensor $\mathbf{S}$ in terms of their derivatives, and stress tensor $\mathbf{T}$ in terms of Hooke's Law:

$$S_{ij} = \frac{1}{2}\left(\frac{\partial u_i}{\partial x_j} + \frac{\partial u_j}{\partial x_i}\right) \tag{B1}$$

$$\Theta = S_{ii} \tag{B2}$$

$$\Sigma_{ij} = \frac{1}{2}[S_{ij} + S_{ji}] - \frac{1}{3}\delta_{ij}\Theta \tag{B3}$$

$$T_{ij} = -K\Theta\delta_{ij} - 2\mu\Sigma_{ij}. \tag{B4}$$

Here we have $x^j = (x, y, z)$, with Latin indices (like i and j) running from 1 to 3. Within any layer, it is straightforward to write down the most general solution of the elasticity equilibrium equation

$$T_{ij,j} = 0 \tag{B5}$$

as

$$\tilde{u}_x = ik_x[(\tilde{\alpha}_+ + \kappa z\tilde{\beta}_+)e^{\kappa z} + (\tilde{\alpha}_- - \kappa z\tilde{\beta}_-)e^{-\kappa z}] - ik_y[\tilde{\gamma}_+e^{\kappa z} + \tilde{\gamma}_-e^{-\kappa z}] \tag{B6}$$

$$\tilde{u}_y = ik_y[(\tilde{\alpha}_+ + \kappa z\tilde{\beta}_+)e^{\kappa z} + (\tilde{\alpha}_- - \kappa z\tilde{\beta}_-)e^{-\kappa z}] + ik_x[\tilde{\gamma}_+e^{\kappa z} + \tilde{\gamma}_-e^{-\kappa z}] \tag{B7}$$

$$\tilde{u}_z = -\kappa[\tilde{\alpha}_+ + \tilde{\beta}_+(-3 + 4\sigma + \kappa z)]e^{\kappa z} + \kappa[\tilde{\alpha}_- + \tilde{\beta}_-(-3 + 4\sigma - \kappa z)]e^{-\kappa z} \tag{B8}$$

where tilde denotes quantities in the x-y spatial-frequency domain, and $\kappa = \sqrt{k_x^2 + k_y^2}$. Namely

$$u_x(x, y, z) = \int \frac{dk_x dk_y}{(2\pi)^2}\tilde{u}(k_x, k_y, z)e^{-i(k_x x + k_y y)}. \tag{B9}$$

We now consider a single-layer coating on a substrate (see Fig. 17), with the coating-substrate interface located at $z = 0$, and the coating-air interface at $z = l$. Suppose there is a force profile $F(x, y)$ exerted perpendicular to the surface at $z = d$, $0 < d < l$, and let us calculate the elastic deformation field caused by F. The entire system is now divided into three regions: (a) at $d < z < l$, (b) at $0 < z < d$, and (s) at $z < 0$. At the interfaces, we obtain the following 15 boundary conditions:

$$T^a_{iz} = 0, \qquad z = l \tag{B10}$$

$$T^a_{xz} = T^b_{xz}, \qquad T^a_{yz} = T^b_{yz}, \qquad T^b_{zz} - T^a_{zz} = F, \qquad z = d \tag{B11}$$

$$u^a_j = u^b_j, \qquad z = d \tag{B12}$$

$$T^b_{iz} = 0, \qquad u^b_j = u^s_j, \qquad z = 0 \tag{B13}$$

as well as the condition that when $z \to -\infty$, $u^s_j \to 0$ (which leads to $\tilde{\alpha}^s_- = \tilde{\beta}^s_- = \tilde{\gamma}^s_- = 0$). We are left with 15 fields

$$(\tilde{\alpha}^a_\pm, \tilde{\beta}^a_\pm, \tilde{\gamma}^a_\pm, \tilde{\alpha}^b_\pm, \tilde{\beta}^b_\pm, \tilde{\gamma}^b_\pm, \tilde{\alpha}^s_+, \tilde{\beta}^s_+, \tilde{\gamma}^s_+) \tag{B14}$$

which can be solved from the 15 boundary conditions. Assuming $\kappa d \ll 1$ and $\kappa l \ll 1$, we find that all $\tilde{\gamma}$ vanish, and

$$\tilde{\alpha}^{\,a}_{\,+} = \frac{F(1 + \sigma_s)[2 - 3\sigma_s + \sigma_c(-3 + 4\sigma_s)]}{2Y_s\kappa^2(-1 + \sigma_c)} \tag{B15}$$

$$\tilde{\alpha}^{\,a}_{\,-} = \frac{F(\sigma_c - \sigma_s)(1 + \sigma_s)}{2Y_s\kappa^2(-1 + \sigma_c)} \tag{B16}$$

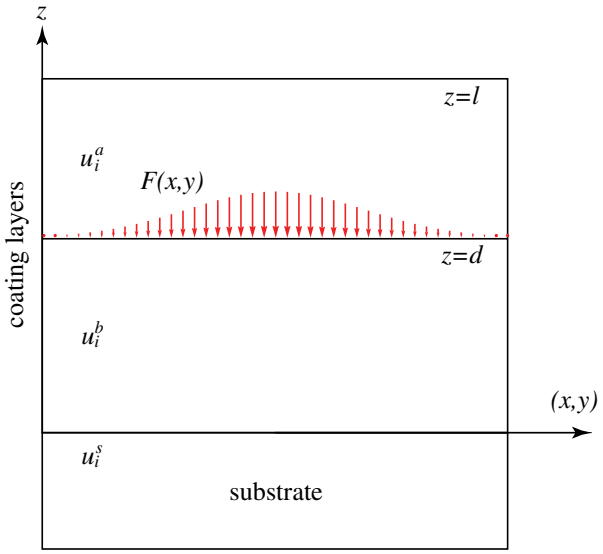

FIG. 17 (color online). Sample with single-layer coating, force is applied perpendicular to the air/coating interface.

$$\tilde{\beta}^a_+ = -\frac{F(1 + \sigma_s)(-3 + 4\sigma_s)}{4Y_s\kappa^2(-1 + \sigma_c)} \tag{B17}$$

$$\tilde{\beta}^a_- = \frac{F(1 + \sigma_s)}{4Y_s\kappa^2(1 - \sigma_c)} \tag{B18}$$

$$\tilde{\alpha}^b_+ = \frac{F(1 + \sigma_s)[2 - 3\sigma_s + \sigma_c(-3 + 4\sigma_s)]}{2Y_s\kappa^2(-1 + \sigma_c)} \tag{B19}$$

$$\tilde{\alpha}^{\,b}_{\,-} = \frac{F(\sigma_c - \sigma_s)(1 + \sigma_s)}{2Y_s\kappa^2(-1 + \sigma_c)} \tag{B20}$$

$$\tilde{\beta}^b_+ = \frac{F[Y_s(1 + \sigma) - Y_c(-3 + \sigma_s + 4\sigma_s^2)]}{4YY_s\kappa^2(-1 + \sigma_c)} \tag{B21}$$

$$\tilde{\beta}^b_- = \frac{F[Y_s(1 + \sigma_c) - Y_c(1 + \sigma_s)]}{4YY_s\kappa^2(-1 + \sigma_c)} \tag{B22}$$

$$\tilde{\alpha}^s_+ = \frac{F(1 + \sigma_s)(-1 + 2\sigma_s)}{Y_s\kappa^2} \tag{B23}$$

$$\tilde{\beta}^s_+ = -\frac{F(1 + \sigma_s)}{Y_s\kappa^2}. \tag{B24}$$

We can therefore obtain the strain tensor in the frequency domain for the coating. The nonzero elements for region (a) are given by

$$S^a_{xx} = \frac{Fk_x^2(-1 + 2\sigma_s)(1 + \sigma_s^2)}{Y_s\kappa^2} \tag{B25}$$

$$S^a_{yy} = \frac{Fk_y^2(-1 + 2\sigma_s)(1 + \sigma_s^2)}{Y_s\kappa^2} \tag{B26}$$

$$S^a_{xy} = S_{yx} = \frac{Fk_xk_y(-1+2\sigma_s)(1+\sigma_s^2)}{Y_s\kappa^2} \tag{B27}$$

$$S^a_{zz} = F\frac{\sigma_c(-1+\sigma_s+2\sigma_s^2)}{Y_s(-1+\sigma_c)} \tag{B28}$$

while those in region (b) are given by

$$S^b_{xx} = \frac{Fk_x^2(-1+2\sigma_s)(1+\sigma_s^2)}{Y_s\kappa^2} \tag{B29}$$

$$S^b_{yy} = \frac{Fk_y^2(-1+2\sigma_s)(1+\sigma_s^2)}{Y_s\kappa^2} \tag{B30}$$

$$S^b_{xy} = S_{yx} = \frac{Fk_xk_y(-1+2\sigma_s)(1+\sigma_s^2)}{Y_s\kappa^2} \tag{B31}$$

$$S^b_{zz} = F\left[\frac{-(1+2\sigma_c)}{Y_c} - \frac{\sigma_c(-1+\sigma_s+2\sigma_s^2)}{Y_s(1-\sigma_c)}\right]. \tag{B32}$$

Using linear superposition, as well as taking the appropriate limits of the above solution, it is straightforward to obtain elastic deformations in all the scenarios in Sec. IV, with forces applied on various surfaces, that are used to obtain cross spectra between different noises.

APPENDIX C: DEFINITION OF LOSS ANGLE

In the past [14], the coating loss angle was defined in association with the parallel and perpendicular coating strains. The equation is written as

$$\phi_{\text{coated}} = \phi_{\text{sub}} + \frac{\delta U_\parallel d}{U}\phi_\parallel + \frac{\delta U_\perp d}{U}\phi_\perp \tag{C1}$$

where $\delta U_\parallel$ and $\delta U_\perp$ are the energy density in parallel and perpendicular coating strains

$$\delta U_\parallel = \int_s \frac{1}{2}(S_{xx}T_{xx} + S_{yy}T_{yy})dxdy \tag{C2}$$

$$\delta U_\perp = \int_s \frac{1}{2}S_{zz}T_{zz}dxdy \tag{C3}$$

and where S_{ij} are the strains and T_{ij} are the stresses. While such a definition seems to be compatible with the symmetry of the system, the quantities $\delta U_\parallel$ and $\delta U_\perp$ cannot be used as energy, since in certain scenarios they each can become negative.

For example, suppose we have a cube with surface area of each side A (Poisson's ratio σ, Young's modulus Y), and we uniformly apply two pairs of forces, one pair with magnitude f on opposite yz planes, the other with magnitude F on opposite xy planes, with $f \ll F$, as shown in Fig. 18. According to the definition of Young's modulus and Poisson's ratio, up to leading order in f/F the nonvanishing strains are

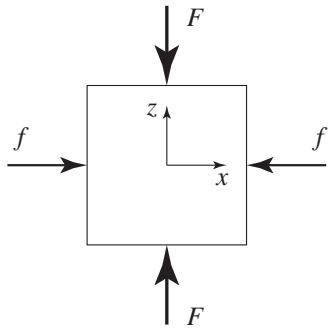

FIG. 18. Solid cube with two pairs of forces applied on the side: $f \ll F$.

$$S_{zz} = -\frac{F/A}{Y}, \qquad S_{xx} = S_{yy} = \sigma\frac{F/A}{Y}. \tag{C4}$$

On the other hand, for stress, we have, up to leading order in f/F,

$$T_{xx} = -f/A, \qquad T_{yy} = 0, \qquad T_{zz} = -F/A. \tag{C5}$$

As a consequence, we have

$$\delta U_\parallel = S_{xx}T_{xx} + S_{yy}T_{yy} = -\sigma fF/(A^2Y) < 0 \tag{C6}$$

which means $\delta U_\parallel$ is not a reasonable candidate for energy, at least with $\sigma \neq 0$. Since it is also true that $S_{xx}T_{xx} < 0$ we will arrive at

$$\delta U_\perp = S_{zz}T_{zz} < 0 \tag{C7}$$

if we take this configuration and rotate by 90 degrees around the y axis, such that x rotates into z.

One reasonable way of defining the loss angle is to derive it from the fundamental elastic energy equation. The general form of the stored elastic energy density U can be written as

$$U = \frac{1}{2}K\Theta^2 + \mu\Sigma_{ij}\Sigma_{ij} \tag{C8}$$

$$U_B = \frac{1}{2}K\Theta^2 \tag{C9}$$

$$U_S = \mu\Sigma_{ij}\Sigma_{ij} \tag{C10}$$

where K is called the *bulk modulus* and μ is the *shear modulus*. In the calculation, we use Young's modulus Y and Poisson's ratio σ instead of K and μ. Their relations are given in Eq. (51). The expansion Θ and shear Σ are both irreducible tensorial parts of the strain tensor S:

$$\Theta = S_{ii} \tag{C11}$$

$$\Sigma = \frac{1}{2}(S_{ij} + S_{ji}) - \frac{1}{3}\delta_{ij}S_{kk}. \tag{C12}$$

Note that the expansion and shear energy U_B and U_S are always positive, so it is consistent to define the loss angles ϕ_B and ϕ_S.

APPENDIX D: ADVANCED LIGO STYLE COATING

In Table VII, we provide the structure of the coating optimized jointly for dichroic operation and thermal noise.

TABLE VII. Structure of an Advanced LIGO-like coating optimized jointly for dichroic operation and thermal noise. The thickness of each layer given in units of wavelength (for light with a vacuum wavelength of 1064 nm) is listed here for the 38 layers. Note that $l_{1,3,5,\ldots}$ are SiO_2 layers, while $l_{2,4,6,\ldots}$ are Ta_2O_5 layers.

j	l_j				
1–5	0.497325	0.208175	0.289623	0.237274	0.250176
6–10	0.245330	0.249806	0.240129	0.270968	0.224129
11–15	0.251081	0.259888	0.260826	0.213460	0.290468
16–20	0.214524	0.273240	0.230905	0.259924	0.230020
21–25	0.275429	0.233086	0.270385	0.208581	0.273798
26–30	0.249741	0.267864	0.204698	0.292317	0.209712
31–35	0.278560	0.220264	0.282694	0.221687	0.268559
36–38	0.233460	0.270419	0.223050		

[1] D. Meiser, J. Ye, D. Carlson, and M. Holland, Phys. Rev. Lett. **102**, 163601 (2009).
[2] LIGO Scientific Collaboration, Rep. Prog. Phys. **72**, 076901 (2009).
[3] G. M. Harry (LIGO Scientific Collaboration), Classical Quantum Gravity **27**, 084006 (2010).
[4] B. Willke *et al.*, Classical Quantum Gravity **23**, S207 (2006).
[5] The Virgo Collaboration, Report No. VIR027A09, 2009 (unpublished).
[6] K. Kuroda (LCGT Collaboration), Classical Quantum Gravity **27**, 084004 (2010).
[7] E. D'Ambrosio, Phys. Rev. D **67**, 102004 (2003); M. Bondarescu and K. S. Thorne, Phys. Rev. D **74**, 082003 (2006); M. Bondarescu, O. Kogan, and Y. Chen, Phys. Rev. D **78**, 082002 (2008).
[8] G. Lovelace, Classical Quantum Gravity **24**, 4491 (2007); J.-Y. Vinet, Living Rev. Relativity **12**, 5 (2009).
[9] H. J. Kimble, B. L. Lev, and J. Ye, Phys. Rev. Lett. **101**, 260602 (2008).
[10] M. Evans, S. Ballmer, M. Fejer, P. Fritschel, G. Harry, and G. Ogin, Phys. Rev. D **78**, 102003 (2008).
[11] G. González and P. Saulson, J. Acoust. Soc. Am. **96**, 207 (1994).
[12] Y. Levin, Phys. Rev. D **57**, 659 (1998).
[13] H. B. Callen and T. A. Welton, Phys. Rev. **83**, 34 (1951).
[14] G. M. Harry, A. M. Gretarsson, P. R. Saulson, S. E. Kittelberger, S. D. Penn, W. J. Startin, S. Rowan, M. M. Fejer, D. R. M. Crooks, G. Cagnoli, J. Hough, and N. Nakagawa, Classical Quantum Gravity **19**, 897 (2002).
[15] A. E. Villar *et al.*, Phys. Rev. D **81**, 122001 (2010).
[16] A. Gurkovsky and S. Vyatchanin, Phys. Lett. A **374**, 3267 (2010).
[17] N. M. Kondratiev, A. G. Gurkovsky, and M. L. Gorodetsky, Phys. Rev. D **84**, 022001 (2011).
[18] L. D. Landau and E. M. Lifshitz, *Theory of Elasticity*, Course of Theoretical Physics (Pergamon, New York, 1981).
[19] I. W. Martin, Classical Quantum Gravity **27**, 225020 (2010).
[20] G. M. Harry *et al.*, Classical Quantum Gravity **24**, 405 (2007).
[21] S. D. Penn *et al.*, Classical Quantum Gravity **20**, 2917 (2003).
[22] G. Billingsley (private communication).
[23] R. Waynant and M. Ediger, *Electro-Optics Handbook* (McGraw-Hill, New York, 1994).
[24] M. M. Fejer, S. Rowan, G. Cagnoli, D. R. M. Crooks, A. Gretarsson, G. M. Harry, J. Hough, S. D. Penn, P. H. Sneddon, and S. P. Vyatchanin, Phys. Rev. D **70**, 082003 (2004).
[25] P. J. Martin, A. Bendavid, M. Swain, R. P. Netterfield, T. J. Kinder, W. G. Sainty, D. Drage, and L. Wielunski, Thin Solid Films **239**, 181 (1994).
[26] G. M. Harry, M. R. Abernathy, A. E. Becerra-Toledo, H. Armandula, E. Black, K. Dooley, M. Eichenfield, C. Nwabugwu, A. Villar, D. R. M. Crooks, G. Cagnoli, J. Hough, C. R. How, I. MacLaren, P. Murray, S. Reid, S. Rowan, P. H. Sneddon, M. M. Fejer, R. Route, S. D. Penn, P. Ganau, J. M. Mackowski, C. Michel, L. Pinard, and A. Remillieux, Classical Quantum Gravity **24**, 405 (2007).
[27] S. D. Penn, P. H. Sneddon, H. Armandula, J. C. Betzwieser, G. Cagnoli, J. Camp, D. R. M. Crooks, M. M. Fejer, A. M. Gretarsson, G. M. Harry, J. Hough, S. E. Kittelberger, M. J. Mortonson, R. Route, S. Rowan, and C. C. Vassiliou, Classical Quantum Gravity **20**, 2917 (2003).
[28] Y. Nakagawa and S. Murashima, Electronics and Communications in Japan **84**, 46 (2001).
[29] J. Stone, J. Lightwave Technol. **6**, 1245 (1988).
[30] J. Agresti, G. Castaldi, R. DeSalvo, V. Galdi, V. Pierro, and I. M. Pinto, Report No. LIGO-P060027-00-Z (unpublished).

[31] J. A. Nelder and R. J. Mead, Computer Journal (UK) **7**, 308 (1965).
[32] W. H. Press, S. A. Teukolsky, W. T. Vetterling, and B. P. Flannery, *Numerical Recipes: The Art of Scientific Computing* (Cambridge University Press, Cambridge, England, 2007), 3rd ed., Sec. 10.5.
[33] A. Heptonstall, G. Cagnoli, J. Hough, and S. Rowan, Phys. Lett. A **354**, 353 (2006).
[34] S. D. Penn, A. Ageev, D. Busby, G. M. Harry, A. M. Gretarsson, K. Numata, and P. Willems, Phys. Lett. A **352**, 3 (2006).
[35] L. H. Donnell, NACA Report No. 479, 1933 (unpublished).
[36] Robert D. Blevins, *Formulas for Natural Frequency and Mode Shape* (Van Nostrand Reinhold Company, New York, 1979).
[37] W. Flügge, *Stresses in Shells* (Springer-Verlag, New York, 1973).
[38] V. B. Braginsky, M. L. Gorodetsky, and S. P. Vyatchanin, Phys. Lett. A **271**, 303 (2000).
[39] D. F. Nelson and M. Lax, Phys. Rev. Lett. **24**, 379 (1970).